

# MC-NeRF: Multi-Camera Neural Radiance Fields for Multi-Camera Image Acquisition Systems

Yu Gao<sup>1,2</sup>, Lutong Su<sup>1,2</sup>, Hao Liang<sup>1,2</sup>, Yufeng Yue<sup>1,2</sup>, Yi Yang<sup>1,2\*</sup>, Mengyin Fu<sup>1,2</sup>

**Abstract**—Neural Radiance Fields (NeRF) use multi-view images for 3D scene representation, demonstrating remarkable performance. As one of the primary sources of multi-view images, multi-camera systems encounter challenges such as varying intrinsic parameters and frequent pose changes. Most previous NeRF-based methods assume a unique camera and rarely consider multi-camera scenarios. Besides, some NeRF methods that can optimize intrinsic and extrinsic parameters still remain susceptible to suboptimal solutions when these parameters are poor initialized. In this paper, we propose MC-NeRF, a method that enables joint optimization of both intrinsic and extrinsic parameters alongside NeRF. The method also supports each image corresponding to independent camera parameters. First, we tackle coupling issue and the degenerate case that arise from the joint optimization between intrinsic and extrinsic parameters. Second, based on the proposed solutions, we introduce an efficient calibration image acquisition scheme for multi-camera systems, including the design of calibration object. Finally, we present an end-to-end network with training sequence that enables the estimation of intrinsic and extrinsic parameters, along with the rendering network. Furthermore, recognizing that most existing datasets are designed for a unique camera, we construct a real multi-camera image acquisition system and create a corresponding new dataset, which includes both simulated data and real-world captured images. Experiments confirm the effectiveness of our method when each image corresponds to different camera parameters. Specifically, we use multi-cameras, each with different intrinsic and extrinsic parameters in real-world system, to achieve 3D scene representation without providing initial poses. The Code and supplementary materials are available at <https://in2-viaun.github.io/MC-NeRF>

**Index Terms**—NeRF, Multi-camera system, intrinsic parameters estimation, pose estimation, 3D scene representation, volume rendering.

## 1 Introduction

Visual 3D reconstruction is pivotal in security surveillance, facial reconstruction, entertainment and robotics. These applications often involve scenes with multi-camera image acquisition systems, providing a wealth of visual information through multi-view perspectives, such as multi-view surveillance systems and facial image capture systems.

Recently, Neural Radiance Field (NeRF)[1] has shown remarkable capabilities in high-quality 3D scene representation. An important precondition for NeRF series methods is the acquisition of images from different views. These images often

\*This work was partly supported by National Natural Science Foundation of China (Grant No. NSFC 62233002, 61973034, U1913203 and CJSP Q2018229)

<sup>1</sup>School of Automation, Beijing Institute of Technology, Beijing, China

<sup>2</sup>State Key Laboratory of Intelligent Control and Decision of Complex System, Beijing Institute of Technology, Beijing, China

\*Corresponding author: Y. Yang Email: yang\_yi@bit.edu.cn

Multi-Camera Images Without Intrinsic and Extrinsic Parameters

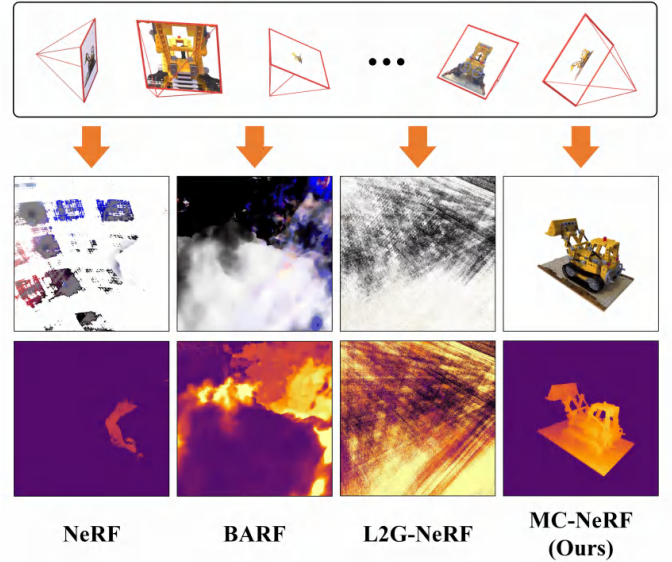


Fig. 1: We introduce MC-NeRF, which can jointly optimize camera parameters with NeRF. Different from other joint optimization methods, MC-NeRF breaks the assumption of unique camera and does not require providing initial camera parameters.

need to be captured using a unique camera, ensuring uniform camera intrinsic parameters across all images. Specifically, widely utilized NeRF datasets, like Synthesis[1], LLFF[2], NSVF[3], and Mip-NeRF 360[4], employ unique camera intrinsic parameters for each scene, ensuring the ray distribution model is fixed in rendering process.

However, in multi-camera image acquisition systems, ensuring that all images are captured by a unique camera is not feasible. When using images captured from these systems for reconstruction based on NeRF methods, the following challenges are encountered: Firstly, each image captured by the system corresponds to different intrinsic and extrinsic parameters, which breaks the assumption of camera uniqueness in the NeRF series methods. Secondly, accurately obtaining the parameters of each camera is time-consuming and involves a significant amount of work, and this calibration process must be repeated whenever any camera in the system changes.

A straightforward solution is using Structure-from-Motion (SfM) methods such as COLMAP[5] to estimate camera parameters, but these techniques can be brittle and failed, especially with sparse or wide-baseline views[6]. Moreover, the

camera parameters obtained by COLMAP represent equivalent camera parameters and cannot restore the real-world scale as parameters obtained through calibration.

Another feasible solution involves NeRF methods that jointly optimize camera parameters, such as SC-NeRF[7], NeRF--[8], L2G-NeRF[9], and BARF[10]. However, these methods still remain susceptible to suboptimal solutions when parameters are poor initialized. Besides, these methods also follow the assumption of a unique camera, which conflicts with the first challenge. Simply changing the assumption from a unique camera to a multi-camera setup introduces a new challenge, known as the coupling issue.

Focusing on the challenges, we introduce Multi-Camera NeRF (MC-NeRF), a novel 3D reconstruction method for multi-camera image acquisition systems. This method uniquely enables reconstruction using a composite of images captured by various cameras, achieving joint optimization of NeRF alongside all camera parameters. To overcome both the susceptible to suboptimal solutions and coupling issue, MC-NeRF adopts auxiliary images containing Apriltags that can simply be obtained from multi-camera image acquisition system instead of rough initial camera parameters.

As for the datasets, the majority of existing NeRF datasets are generated based on a unique camera, which can not satisfy the requirement of randomized camera parameters with mixed cameras. This has motivated us to propose our own dataset. The MC dataset provides the reader with the flexibility to tailor camera parameters and the number of cameras, allowing for free combinations. Furthermore, to demonstrate the effectiveness of our method in real-world applications, we constructed a multi-camera image acquisition system comprising 88 cameras and provided a dataset from real-world scenarios.

In conclusion, the contributions of this paper are as follows:

- We address the coupling issue within joint optimization of intrinsic and extrinsic parameters and the degenerated cases in intrinsic parameter estimation.
- We propose a joint optimization strategy that can simultaneously optimize the intrinsic parameters, extrinsic parameters and neural radiation fields.
- We construct a multi-camera image acquisition system comprising 88 cameras and provided a new dataset of real-world scenes captured by this system.
- We provide a new simulated dataset for multi-camera acquisition systems including the source code for dataset generation, enabling readers to create their own datasets freely.

## 2 RELATED WORK

**Camera Calibration** The camera model demonstrates how points in camera coordinates are projected into pixel coordinates, and camera calibration aims to determine the parameters within this model. Earlier calibration methods observe calibration objects whose geometry in 3D space is known with high precision to calculate the camera parameters, and this efficient method requires only a small number of images to achieve high-performance results[11]. Considering the precision of manufacturing and the cost of calibration objects, Tsai et al. [12] captured images of a 2D planar calibration object from

various poses to estimate camera parameters. This method requires providing accurate pose for each calibration plane. Another widely used approach adopting 2D planar calibration is the chessboard method proposed by Zhang[13]. This technique involves capturing images including a chessboard pattern from different positions to determine the camera parameters. Compared with Tsai's method, Zhang's approach eliminates the need to provide the calibrator's position. In addition to employing known calibration points, there are also some methods relying on detecting specific features to achieve calibration, like vanishing points[14], [15] and coplanar circles[16].

In recent years, deep learning has provided new inspirations for camera calibration. DeepCalib[17] utilizes a CNN network trained with a vast collection of scene images matched with corresponding camera parameters, and established the relationship between image features and camera parameters. DeepCalib can directly predict calibration results based on the input images. An advantage of this method is that there is no need to provide typical calibration objects. Similar to DeepCalib, Hold-Geoffroy et al.[18] also attempted to predict camera parameters directly from a single image, and they explored the boundaries of human tolerance towards image distortion, and further designed a new perceptual measure for the calibration errors.

Apart from methods designed explicitly to obtain calibration results, some works can indirectly acquire camera parameters. Some learning methods[19]–[26] rely on classical multi-view geometry theories, like epipolar constraints, PnP (Perspective-n-Point) algorithms, feature points matching and triangulation, to achieve 3D reconstruction or visual odometry. Although these applications may not design for obtaining camera parameters, they still have the capability to retrieve poses, and the mentioned theories always serve as the foundation for model block design and loss functions design. Additionally, camera pose estimation methods based on NeRF, such as iNeRF[27], have also emerged.

**Camera Preconditions of NeRF** Acquiring accurate camera parameters can often be challenging, and in some cases, certain parameters might even be unreachable. When camera parameters are unreliable, adopting classic NeRF-series methods[28]–[36] to describe the scene becomes difficult. Some researches[37]–[39] employ input images to estimate camera poses. Li et al.[29] used COLMAP to obtain the initial camera poses, which were subsequently used as precondition for NeRF to reconstruct the scene. Instead of using existing methods directly, some other methods[8], [10], [40], [41] can leverage prior knowledge to establish the loss function by introducing geometric constraints with photometric consistency. Specifically, Wang et al.[8] jointly optimized camera parameters and NeRF through photometric reconstruction. Jeong et al[7] design a mixed camera model to achieve the self-calibration, and the process is constrained by geometric and photometric consistency for NeRF training. Lin et al[10] employed a coarse-to-fine auxiliary positional embedding[42]–[44] to jointly recover the radiance field and camera pose. NoPe-NeRF[45] uses monocular depth priors to constrain the scene as well as relative pose estimates. Ray-to-ray correspondence losses also can be leveraged to impose constraints on the

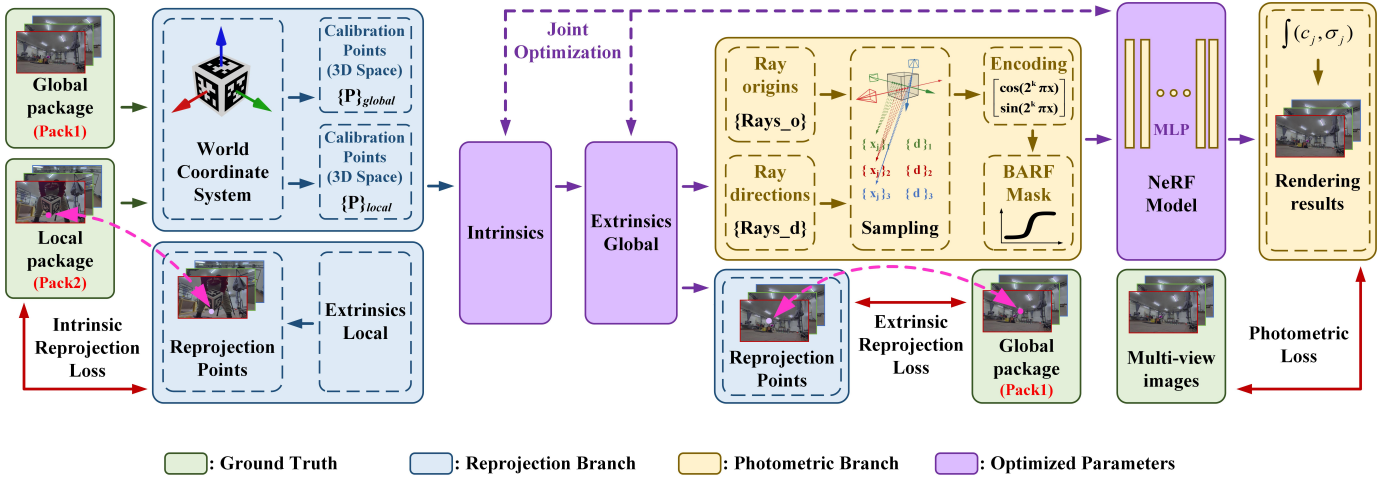


Fig. 2: Overview of the proposed method. First, based on the designed process (as shown in Fig. 5), we obtain two sets of auxiliary images containing AprilTags, named *Pack1* and *Pack2*. These image sets provide 3D coordinates in the world coordinate system and feature point coordinates in the images, which are utilized to establish reprojection loss functions. Second, the camera’s intrinsic and extrinsic parameters, which are constrained by the reprojection loss function, are used to generate sampling points. These points are then fed into a Multilayer Perceptron (MLP) that employs BARF-based progressive encoding for subsequent training.

relative pose estimates by utilizing either keypoint matches or dense correspondences[7], [46]. DBARF[47] adopts low-frequency feature maps to guide the bundle adjustment for generalizable NeRFs[48], [49]. GNeRF[50] introduces a pose estimator to directly estimate camera poses from images. Essentially, these methods combine the training process with camera parameters prediction.

In summary, NeRF series methods have been extensively explored and significantly improved, yet certain limitations remain. Firstly, previous works often require inputs collected from the same camera or cameras with identical performance, which is difficult to ensure in a multi-camera image acquisition system. Secondly, different intrinsic parameters are rarely considered in prior researches, implying that existing methods aim to standardize all images to a single camera model with uniform parameters.

### 3 METHOD

#### 3.1 Overview

The proposed method, illustrated in Fig.2, consists of three loss functions and is divided into two branches. As a downstream component in the workflow, the rendering network is susceptible to fluctuations in upstream inputs, suggesting that training the rendering network could be ineffective when camera parameters change drastically. Moreover, the number of optimized parameters in the photometric loss branch far exceeds that of the intrinsic and extrinsic reprojection loss branches, which prolongs the training duration. Therefore, initializing camera parameters and subsequently refining them during rendering network training emerges as an efficient approach.

#### 3.2 Multi-Camera System Design and Data Acquisition

In this section, we first introduce the multi-camera image acquisition system we constructed in the real world and the real-scene data captured. Next, we present the proposed synthetic datasets, which simulates scenarios in four different styles, including our room system. Finally, we explain why using images containing AprilTags in our method is both necessary and feasible.

##### 3.2.1 Multi-Camera Image Acquisition System

The motivation for this work comes from the multi-camera image acquisition system constructed by ourselves. The dimensions of our site are a rectangular area measuring  $9\text{m} \times 6\text{m} \times 2.4\text{m}$ . There are a total of 88 different cameras, each with independent camera parameters. Based on our experience, the calibration parameters of one camera cannot be shared with others, even though these cameras are claimed to be of the same model. The cameras are mounted on the truss in a uniform distribution, aligning with the setup commonly found in multi-camera image acquisition systems, such as facial imaging and motion capture systems. Fig.3. shows the detailed information of our site, as well as the scene data captured using our system.

##### 3.2.2 Multi-Camera Synthetic Datasets

We designed four datasets based on commonly used multi-camera image acquisition systems. The camera distribution in these datasets includes halfball style (as employed by the original NeRF), ball style, room style, and array style. The datasets contain a total of 32 groups, with 8 different objects for each dataset style. The different sampling styles involve varying numbers of cameras, leading to different numbers of training images. The details of the datasets are illustrated in Section 4.1.

It’s worth noting that due to the images being collected from cameras with different intrinsic parameters, determining





Fig. 3: Multi-camera image acquisition system in real-world and captured images containing AprilTags. The left side details the dimensions of our experimental site and the camera setup, utilizing a total of 88 cameras across the scene. The right side presents the real-world scene data we collected, divided into two sets. Consistent with the descriptions in Fig.2, *Pack1* represents the Global package, while *Pack2* represents the Local package. Because the site covered by the cameras is also the scene for NeRF representation, we use the images in Package1 for training.

which camera to use for generating the test data is challenging. To showcase the performance of the proposed method across various camera intrinsic parameters, we generate the 200 test images in each group by continuously varying the intrinsic parameters along the camera’s motion trajectory. Detailed sampling procedures and parameter variations have been provided on the project website.

### 3.2.3 Images with AprilTags

Our method, compared to previous works, requires additional images containing AprilTags. This necessity arises from the new challenges posed by each image corresponding to independent camera parameters.

To address this problem, we introduce additional constraints to establish the relationship for all images. AprilTag is chosen because they provide high-quality and stable geometric constraints. Because of these constraints, images containing AprilTags are integrated throughout the entire training process, rather than obtaining initial values and then discarding them.

Regarding feasibility, proposed method is compatible with many of commonly used multi-camera image acquisition systems, including motion capture systems, facial image capture systems, and multi-view surveillance systems, among others. In these setups, cameras are statically positioned and requiring installation in advance. Given these conditions, capturing images containing AprilTags is practical and achievable.

## 3.3 Multi-Camera Intrinsic Parameters Estimation

In this section, we first present the method for obtaining intrinsic parameters. Then, we show how we design optimized parameters. Next, we analyze the degenerate cases during intrinsic parameter optimization. Lastly, based on the degenerate cases, we discuss the scheme and usage of the calibration object.

### 3.3.1 Intrinsic parameters estimation

The process of computing the camera intrinsic parameters is called calibration. The problem can be described as: given  $n$  calibration points  $P_i (i = 0, 1, 2, \dots, n)$  in world coordinate system with corresponding pixel coordinates labelled  $p_i$ , determining the intrinsic matrix  $K$  of the pinhole camera. For the same camera, the projection relationship between  $P_i$  and  $p_i$  is as follows:

$$sp_i = K [R|T] P_i \quad \text{with } K = \begin{bmatrix} \alpha & c & u_0 \\ 0 & \beta & v_0 \\ 0 & 0 & 1 \end{bmatrix} \quad (1)$$

where  $s$  is an arbitrary scale factor,  $[R|T]$  are the extrinsic parameters, and  $K$  is defined as the camera intrinsic matrix.  $(u_0, v_0)$  in  $K$  are the coordinates of the principal point,  $\alpha$  and  $\beta$  are called scale factors in image  $u$  and  $v$  axes respectively, and  $c$  describes the skewness of the two image axes. We define a homography  $H$  with size  $3 \times 4$ , which is also called camera matrix, and we have:

$$sp_i = H P_i \quad \text{with } H = K [R|T] \quad (2)$$

with the condition of  $n \geq 6$  and  $\|H\|_F = 1$ , where  $F$  is Frobenius norm,  $H$  can be solved by SVD decomposition. When  $H$  is obtained,  $K$  and  $R$  can be solved by the first three columns of  $H$ . Considering that  $K$  and  $R$  are upper triangular matrix and orthogonal matrix respectively, we can adopt  $RQ$  decomposition to get the solutions. Generally, we define the camera coordinate system as same as it defined in OpenCV, and the diagonal elements of  $K$  are all positive, then we have:

$$K = KD \quad \text{with } D = \begin{bmatrix} f(K_{11}) & 0 & 0 \\ 0 & f(K_{12}) & 0 \\ 0 & 0 & f(K_{13}) \end{bmatrix} \quad (3)$$

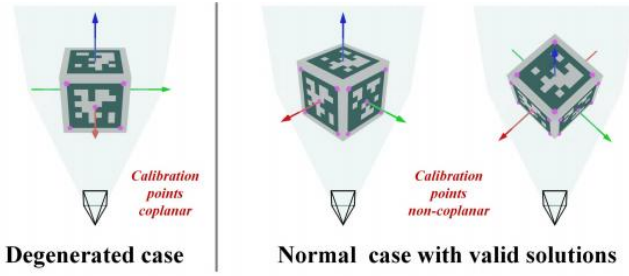


Fig. 4: Degenerate case in intrinsic parameters estimation. When a single AprilTag is present in the calibration image, obtaining a valid solution is not feasible. At least two AprilTags ensures the acquisition of camera intrinsic parameters.

where  $f(x)$  is the sign function  $sign(x)$ . Besides, we set the condition of  $\|H\|_F = 1$ , which is not the real scale of  $K$ . The final camera intrinsic matrix is defined as  $K = K/K_{33}$ .

### 3.3.2 Training Parameters and Degenerated Case

The goal of the optimization process is to reproduce the computing of Eq.(1). The equation satisfies both the projection mapping and the inverse projection mapping. We choose the inverse projection mapping as the reproduction computation flow because it doesn't require depth information for precise 2D coordinate retrieval, and the loss function can be implemented in pixel coordinate system.

Assume that the multi-camera system contains  $m$  cameras with unknown parameters, and  $K_j (j = 0, 1, 2, \dots, m)$  denotes the intrinsic matrix of each camera.

We decompose  $K_j$  into the initialization  $K_{j0}$  and the adjustable weights  $\Delta K_{j0}$ , and also assume the axes of the image coordinate system are all perpendicular to each other, which means  $c = 0$ . The matrix:

$$K_j = \begin{bmatrix} f_{xj} \cdot \Delta f_{xj} & 0 & u_{0j} \cdot \Delta u_{0j} \\ 0 & f_{yj} \cdot \Delta f_{yj} & v_{0j} \cdot \Delta v_{0j} \\ 0 & 0 & 1 \end{bmatrix} \quad (4)$$

We define the adjustable extrinsic parameters in the  $se(3)$  space and then convert back to the  $SE(3)$  space. Let  $[\alpha_{j0}, \alpha_{j1}, \alpha_{j2}, \alpha_{j3}, \alpha_{j4}, \alpha_{j5}] (j = 0, 1, 2, \dots, m)$  be 6 adjustable parameters in the  $se(3)$  and the corresponding matrix in the  $SE(3)$  is denoted as  $[R_j | T_j]$  with size  $3 \times 4$ . For every camera in the system, we have:

$$pd\_p_{ij} = K_j [R_j | T_j] P_{ij} \quad (5)$$

where  $P_{ij}$  is the 3D point used as input and generated by the calibration object,  $pd\_p_{ij}$  is the predicted pixel coordinate. We define the loss function for the intrinsic parameters estimation stage as:

$$loss_{intr} = \sum_{i=0, j=0}^{i=n, j=m} \left\| \frac{gt\_p_{ij}}{\sqrt{h^2 + w^2}} - \frac{pd\_p_{ij}}{\sqrt{h^2 + w^2}} \right\|_2^2 \quad (6)$$

where  $h, w$  represent the height and width of the image, and  $gt\_p_{ij}$  denotes the ground-truth coordinate of  $p_{ij}$ , which can be detected in the images including the calibration object.

It should be noted that the above optimization cannot obtain an accurate solution when all the feature points in the image

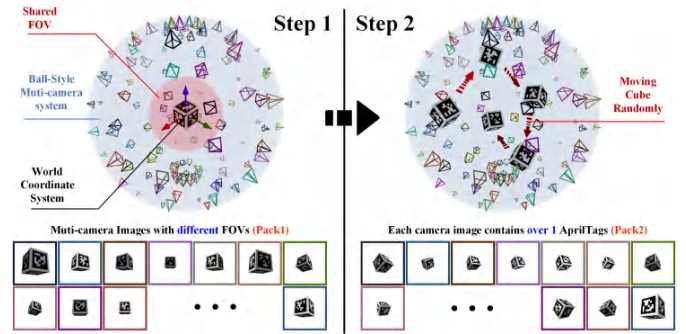


Fig. 5: Details of calibration data Acquisition. Firstly, the cube is captured by all cameras within the shared field of view, with its center defined as the origin of the world coordinate system. We define the set of images captured during this step as *Pack1*. Secondly, to ensure that each camera captures an image containing at least two AprilTags, the cube is moved randomly. The set of images captured in this phase is defined as *Pack2*.

are located on the same plane, because of the degenerated cases [51]. This means that each calibration image needs to contain at least two AprilTags. The specific degenerated case and normal case are shown in Fig.4.

### 3.3.3 Calibration cube design and instruction

Compared to single-camera calibration, multi-camera calibration has the following limitations: First, the cameras of multi-camera systems are fixed in space and cannot move freely. Second, capturing images with the calibrator in the ideal position is time-consuming for multi-camera systems, making it necessary for each camera to complete the calibration using as few images as possible. Third, multi-camera systems need to be calibrated frequently because of the changing of camera position and lens. Besides, calibrator should be designed for ease of manufacturing while maintaining high machining precision to ensure the accuracy of calibration. As mentioned in section 3.3.2, degenerated cases lead the invalid solutions when all calibration points are coplanar. This also requires that the calibrator must have the capability of providing non-coplanar three-dimensional calibration points.

To meet these requirements, we designed the calibrator as a cube. Each side of it is spray-painted with a different AprilTag label from the 36H11 family. AprilTag can provide five calibration points per plane, including four corners and a central point. Detecting more than two AprilTag patterns in each image can provide at least 10 points, which fulfills the condition of being non-coplanar. Besides, the cube is easy to machine, with low cost but high machining accuracy. As for calibration points detection, AprilTag supports an open source algorithm, which is stable and easy to deploy. Fig.5 illustrates the procedure for acquiring calibration data.

## 3.4 Multi-Camera Extrinsic Parameters Estimation

Once the coarse intrinsic parameters are obtained, the estimation for extrinsic parameters is converted into a PNP (Perspective-n-Point) problem. The form of the loss function

in Eq.(6) is extremely similar to that of the Bundle Adjustment (BA) method, which is widely employed to address PnP problem. This means that we can use the reprojection process to optimize the extrinsic parameters again.

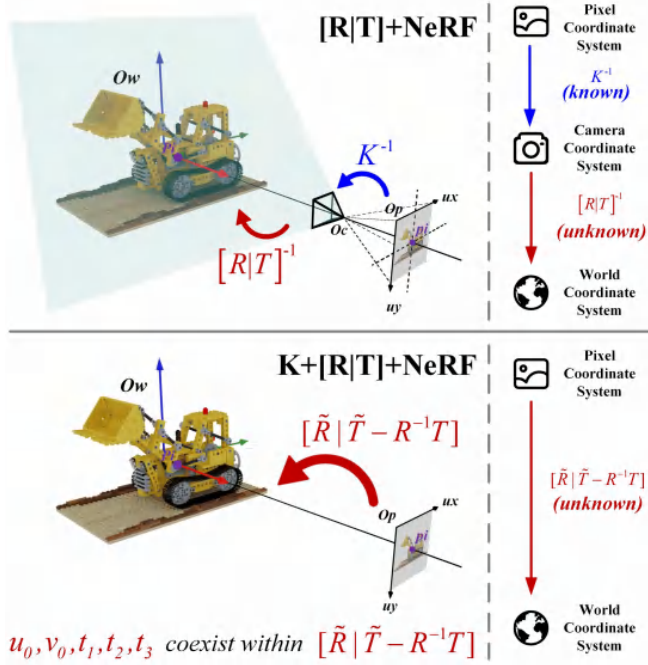


Fig. 6: Coupling issue between intrinsic and extrinsic parameters. 1) The first row illustrates the joint optimization for poses and NeRF. In methods such as BARF or L2G-NeRF, where the intrinsic parameters are known, mitigating the issue of camera parameters coupling. 2) The second row showcases the joint optimization of all parameters, as outlined in Eq.(9). This procedure effectively represents a global transformation involving scaling, rotation, and translation.  $u_0$  and  $v_0$  from intrinsic parameters, along with  $t_1$ ,  $t_2$  and  $t_3$  from extrinsic parameters, coexist within  $\tilde{T} - R^{-1}T$  and cannot be disentangled.

### 3.4.1 World coordinate system

The world coordinate system definitions in *Pack1* and *Pack2* are entirely different. It's important to note that the world coordinate system definition of the multi-camera acquisition system corresponds to that of *Pack1*. The origin of the world coordinate system is defined at the geometric center of the cube. The X-axis points towards the AprilTag labeled with number 1, the Y-axis points towards number 2, and the Z-axis points towards number 4.

When using the *Pack2* data to obtain camera intrinsic parameters, the matching extrinsic parameters can also be obtained. However, due to the random movement of the cube, the world coordinate systems for each image are not consistent with others. As a result, these extrinsic parameters are irrelevant to the multi-camera acquisition system and carry no practical significance. As illustrated in Fig.2, the *Extrinsics Local* from Intrinsic reprojection loss branch is not reused in the subsequent optimization.

### 3.4.2 PnP with bundle adjustment

The Perspective-n-Point (PnP) problem is defined as follows: given a set of 3D points in world coordinate system, and knowing their corresponding coordinates in pixel coordinate system, solving the camera extrinsic parameters with the condition of intrinsic parameters provided. As a typical method to solve PnP, Bundle Adjustment (BA) can be described as to optimize camera poses and scene points by minimizing the difference between the projected 3D scene points in the images and their corresponding 2D image feature points. The loss function in BA is defined as:

$$loss_{BA} = \frac{1}{2} \sum_{i=0, j=0}^{i=n, j=m} \left\| \frac{gt\_p_{ij}}{\sqrt{h^2 + w^2}} - \frac{pd\_p_{ij}}{\sqrt{h^2 + w^2}} \right\|_2^2 \quad (7)$$

Eq.(6) and Eq.(7) differ only in their coefficients, and the computation flow can be reused to regress the extrinsic parameters.

### 3.5 Coupling Issue in Global Optimization

We unfold this section by explaining the coupling issue during joint training of intrinsic and extrinsic parameters. Following this, we validate the proposed method within the 2D image alignment space, which is similar to previous works such as BARF and L2G. We also explain the differences between jointly optimizing all camera parameters and individually optimizing extrinsic parameters in this part. Finally, we present the details of how we design the entire network and transition it from the 2D image alignment space to the 3D space.

#### 3.5.1 Coupling in camera parameters

In the NeRF method, rays are defined by their direction vectors, which implies that we can disregard the scale variable  $s$ . Given pixel coordinates as inputs and  $c = 0$  provided in Eq.(4), Eq.(1) can be rewritten as follows:

$$P_i = [R|T]^{-1} K^{-1} p_i$$

$$\text{with } K = \begin{bmatrix} 1/f_x & 0 & -u_0/f_x \\ 0 & 1/f_y & -v_0/f_y \\ 0 & 0 & 1 \end{bmatrix} \quad (8)$$

Specifically, Eq.(8) can be modified as:

$$\begin{aligned} P_i &= R^{-1} K^{-1} p_i - R^{-1} T \\ \Rightarrow P_i &= \tilde{R} p_i + (\tilde{T} - R^{-1} T) \end{aligned} \quad (9)$$

where  $\tilde{R}$  and  $\tilde{T}$  are as follows:

$$\begin{aligned} \tilde{R} &= \begin{bmatrix} r_{11}/f_x & r_{21}/f_y & r_{31} \\ r_{12}/f_x & r_{22}/f_y & r_{32} \\ r_{13}/f_x & r_{23}/f_y & r_{33} \end{bmatrix}, \\ \tilde{T} &= \begin{bmatrix} -u_0 r_{11}/f_x - v_0 r_{21}/f_y \\ -u_0 r_{12}/f_x - v_0 r_{22}/f_y \\ -u_0 r_{13}/f_x - v_0 r_{23}/f_y \end{bmatrix} \end{aligned} \quad (10)$$



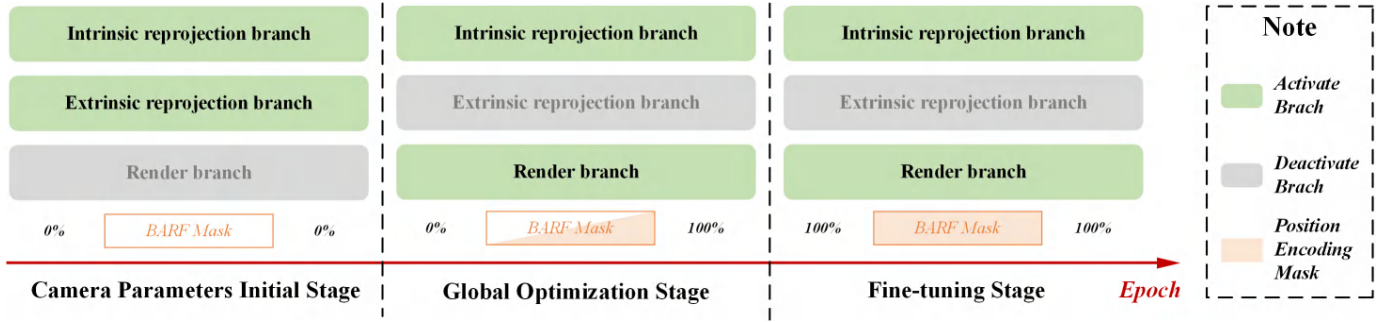


Fig. 7: Training sequential diagram: Our training process consists of three stages: 1) Camera Parameter Initialization Stage: The goal in this stage is to obtain coarse intrinsic and extrinsic parameters. Rendering training is not conducted in this stage. 2) Global Optimization Stage: Due to the coupling issue during joint optimization, we retain the Intrinsic Reprojection branch as a decoupling constraint. We also employ the progressive alignment method proposed in BARF to achieve extrinsic parameters with higher accuracy than those obtained in the first stage. 3) Fine-tuning Stage: In this stage, continuing to optimize extrinsic parameters without the progressive alignment constraint can lead to divergence. We freeze the extrinsic parameters and only adjust the intrinsic parameters.

we also have:

$$\tilde{T} - R^{-1}T = \begin{bmatrix} \tilde{t}_1 r_{11} + \tilde{t}_2 r_{21} + \tilde{t}_3 r_{31} \\ \tilde{t}_1 r_{12} + \tilde{t}_2 r_{22} + \tilde{t}_3 r_{32} \\ \tilde{t}_1 r_{13} + \tilde{t}_2 r_{23} + \tilde{t}_3 r_{33} \end{bmatrix} \quad (11)$$

$$\begin{aligned} \text{with } \tilde{t}_1 &= -u_0/f_x - t_1 \\ \tilde{t}_2 &= -v_0/f_y - t_2 \\ \tilde{t}_3 &= -t_3 \end{aligned}$$

In Eq.(10) and Eq.(11),  $r_{ij}$  represents element of the rotation matrix  $R$  in 3D space, and  $t_i$  represents the element of the translation matrix  $T$  in 3D space. From Eq.(11), we can observe that  $u_0$ ,  $v_0$  and  $t_1$ ,  $t_2$ ,  $t_3$  are strongly coupled. While we can obtain result for  $\tilde{T} - R^{-1}T$  through optimization, distinguishing between  $u_0$ ,  $v_0$  and  $T$  remains challenging.

A straightforward solution to address the coupling issue is imposing additional constraints on the coupled variables. We introduce a constraint for the camera intrinsic parameters to separate intrinsic and extrinsic parameters from each other. In the collected calibration data, *Pack2* provides comprehensive constraints on the camera intrinsic parameters, while *Pack1* only constrains the world coordinate system with extrinsic parameters (the images in *Pack1* cannot guarantee at least two AprilTags captured in each image). The described procedure is shown in Fig.6.

In summary, the intrinsic reprojection loss is required as a constraint to facilitate the independent estimation. In this way, the coupled variables  $u_0$ ,  $v_0$  and  $t_1$ ,  $t_2$ ,  $t_3$  can be separated from each other.

### 3.5.2 Neural Image Alignment (2D)

As mentioned in BARF and L2G-NeRF, 2D neural image alignment problem can be described as: let  $x$  be the 2D pixel coordinates, we aim to optimize a 2D neural field parameterized as the weights of a multilayer perceptron (MLP)  $f_{mlp}$ :

$$RGB(x) = f_{mlp}(Tx; w) \quad (12)$$

while also solving for geometric transformation parameters as  $T = [R|T]$ , and  $[R|T]$  denotes the rigid rotation and translation in 2D space.

Compared to the previously introduced 2D image alignment problem, we have increased its complexity even further, resulting in the updated problem formulation:

$$RGB(x) = f_{mlp}(TLx; w) \quad (13)$$

Where  $L$  represents a linear transformation, simulating the computation flow of projection from pixel coordinates to camera coordinates. The form of  $L$  is consistent with that of the intrinsic matrix  $K$  and is defined as follows:

$$L = \begin{bmatrix} a_1 & 0 & b_1 \\ 0 & a_2 & b_2 \\ 0 & 0 & 1 \end{bmatrix} \quad (14)$$

Based on Eq.(13) and Eq.(14), the estimation for the intrinsic parameter  $K$  can be equivalently represented as the estimation for the linear transformation  $L$ . It's important to note that in the experiments conducted by BARF and L2G, the term  $T$  in Eq.(13) is defined as a homography matrix. However, since the transformation requirements for 3D space in the NeRF series methods involve only rotation and translation, we redefine  $T$  as  $[R|T]$  instead.

### 3.5.3 NeRF with Bundle Adjustment

Lin et al. [10] first proposed Bundle-Adjusting Neural Radiance Fields (BARF), which addresses the problem of achieving NeRF training without precise camera extrinsic parameters. We believe one of the key advantages of BARF is its independence from requiring extra information. It only needs simple adjustments to the coarse-to-fine NeRF architecture to achieve the joint optimization for camera pose and NeRF.

We attempted to extend this method by incorporating the estimation of camera intrinsic parameters into the BARF framework. The training sequence is illustrated in Fig.7. During the camera parameters initialization stage, coarse camera parameters are obtained using the calibration data *Pack1* and *Pack2*. In the global optimization stage, we employ the

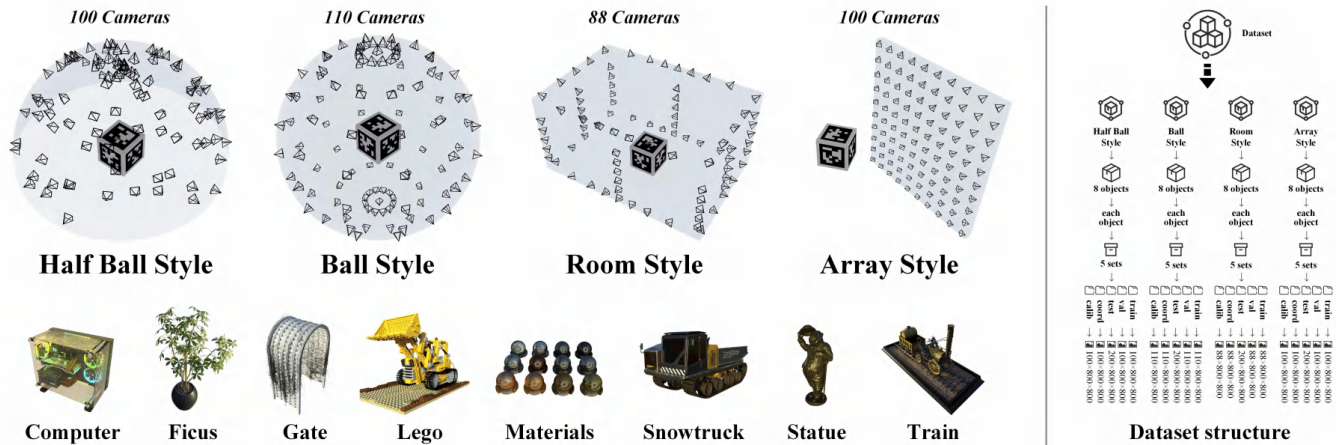


Fig. 8: Scene styles and dataset structure. The left side shows the camera distribution for the different multi-camera systems and the eight objects of interest in our dataset. The right side illustrates the composition of our dataset. Within each style, there are eight objects correspond to five sets of data, including two sets of calibration (*Pack1* and *Pack2*), as well as the training, validation, and test sets.

intrinsic reprojection loss branch to impose constraints on the principal point coordinates of the camera. We leverage the progressive alignment method from BARF to optimize the extrinsic parameters of the multi-camera acquisition system. In the fine-tuning stage, we freeze the extrinsic parameters and only refine the intrinsic parameters to obtain the final results.

## 4 EXPERIMENTS

The goal of the experiments is to answer the following questions:

- 1) Does NeRF still work effectively when each image corresponds to different intrinsic parameters? In comparison to the unique camera assumption in the original NeRF, what challenges do the multiple intrinsic parameters present to the NeRF series methods?
- 2) Does the Intrinsic Reprojection Loss successfully yield accurate camera intrinsic parameters? Section 3.3 highlights that if the calibration points lie on the same plane, a degenerate case could occur. Does this issue still exist in methods based on network optimization?
- 3) Is the extrinsic estimation introduced in Section 3.4 necessary? How does the performance of models such as BARF and L2G-NeRF, which can directly regress extrinsic parameters with accurate intrinsic parameters provided?
- 4) Compared to previous works, how does the proposed method perform in the 2D neural image alignment problem?
- 5) Introduced in Section 3.5, does the approach achieve global optimization for the network? Having obtained the intrinsic and extrinsic parameters of different cameras as initial values in Sections 3.3 and 3.4, how does the performance compare when directly optimizing NeRF using these initial parameters, without implementing global optimization?

- 6) How does the performance of the proposed method compare to simple mixed methods (like off-the-shelf SFM libraries with NeRF) in real-world scenarios?

### 4.1 Dataset and Hardware Platform

The synthetic datasets are generated using Blender 3.3.3, and the intrinsic parameters for each camera within each style are different. For example, in the HalfBall Style acquisition system, there are a total of 100 cameras with varying intrinsic parameters. The training data is collected using these cameras according to their depicted positions. Similarly, the validation data is also collected using these cameras, but each camera's position differs from that of the training set. For each style, the number of validation images is equal to the number of training images. The resolution of each image is  $800 \times 800$ . The details of the datasets are illustrated on the right side of Fig.8.

The real-world dataset are collected using 88 different cameras installed by us, with a resolution of  $1920 \times 1080$ , and each image corresponds to independent camera parameters. To accelerate the training speed, we reduced the image resolution to  $960 \times 540$  for the experiments. All of our experiments were conducted on an NVIDIA RTX 3090 with 24GB, and the PyTorch version used is 1.12.1.

### 4.2 Exp.1 Unique-Camera VS Multi-Cameras

In this experiment, we aim to explore whether NeRF can simultaneously utilize multiple intrinsic parameters, a foundational prerequisite for our method. We select cameras with FOVs of 40, 50, 60, 70, and 80 degrees to generate a mixed dataset. NeRF is then trained on this dataset with the provided ground-truth intrinsic and extrinsic parameters. Simultaneously, we conduct training of NeRF with each FOV data independently to compare the rendering performance against NeRF trained on the mixed dataset. Hence, this experiment



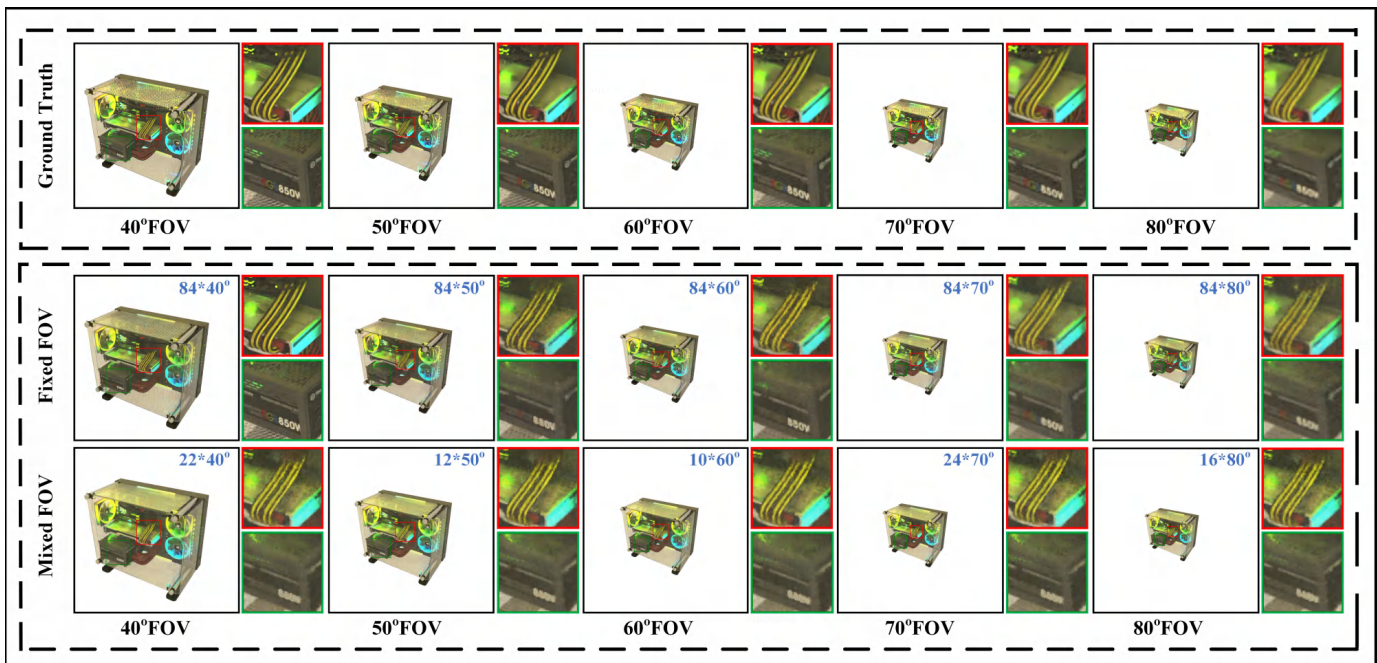


Fig. 9: Comparison of rendering performance in NeRF with mixed intrinsic dataset and single intrinsic dataset. The top row shows ground-truth images captured at varying FOVs, indicated below each image. The second row displays results produced by the NeRF model trained on each fixed FOV dataset, and the third row exhibits results from the NeRF model trained on a mixed dataset. The numbers in the top-right corner of each result represent the number of images in the dataset with the current FOV. In the mixed dataset, there are 22, 12, 10, 24, and 16 images for FOVs of 40, 50, 60, 70, and 80 degrees, respectively.

TABLE 1: Quantitative results of *Exp.1*.

		40°	50°	60°	70°	80°
PSNR↑	Fixed FOV	25.440	27.872	29.896	32.935	34.783
	Mixed FOV	24.169	27.333	29.949	32.138	33.786
	Distance	1.271	0.539	0.053	0.797	0.997
SSIM↑	Fixed FOV	0.858	0.913	0.942	0.969	0.980
	Mixed FOV	0.819	0.899	0.939	0.963	0.975
	Distance	0.039	0.014	0.003	0.006	0.005
LPIPS↓	Fixed FOV	0.108	0.056	0.040	0.017	0.014
	Mixed FOV	0.147	0.069	0.037	0.026	0.016
	Distance	0.039	0.013	0.003	0.009	0.002

comprises a total of 6 datasets: one mixed dataset and five independent datasets, each containing 84 images with identical extrinsic parameters across all datasets.

The comparison results can be observed in Table 1 and Fig.9. The *Distance* item in Table 1 indicates the absolute difference between their respective indicators. As evident from both Table 1 and Fig.9, the models trained with different datasets exhibit nearly equivalent performance. This observation has shown the capability of NeRF that can effectively process multi-camera images, when accurate camera intrinsic and extrinsic parameters are provided.

In summary, with accurate camera parameters provided, NeRF can work efficiently when each image corresponds to different intrinsic parameters. We believe that the challenge posed by multiple intrinsic parameters to NeRF is how to obtain accurate intrinsic parameters for each individual camera. The function of intrinsic and extrinsic parameters is to

establish a mapping between image pixels and spatial rays. The accuracy and correctness of this mapping serve as vital prerequisites for NeRF, irrespective of whether the camera intrinsics are the same or equal.

### 4.3 Exp.2 Intrinsic Parameters Estimation

In this experiment, we aim to verify the effectiveness of the proposed intrinsic parameters estimation method. We conduct experiments using AprilTag images collected by 70 cameras with different FOVs. The dataset consists of three groups: the images in the first group contain only one AprilTag in each image, denoted as *Dataset\_A*. This group ensures that the calibration points lie in the same plane. The images in the second group contain two AprilTags, denoted as *Dataset\_B*. According to the conclusion in Section 3.3, the results trained by this dataset can successfully obtain the intrinsic parameters. The images in the third group contain three AprilTags, denoted as *Dataset\_C*. We believe that the results trained with this group will have better accuracy. Here,  $F_x$  and  $F_y$  are the focal lengths of the camera in the horizontal and vertical directions, while  $u_x$  and  $u_y$  are the coordinates of the principal point.

The results are presented in Fig. 10 and Table 2. Average loss of intrinsic parameters refers to the average absolute error between predicted intrinsic parameters and ground truth intrinsic parameters. In this scenario, the images contain only 1 AprilTag (*Dataset\_A*) and the intrinsic parameters cannot be obtained. This case exhibits similar performance to the degenerate case, indicating the persistence of degeneracy in the proposed method. Specifically, as illustrated by the black

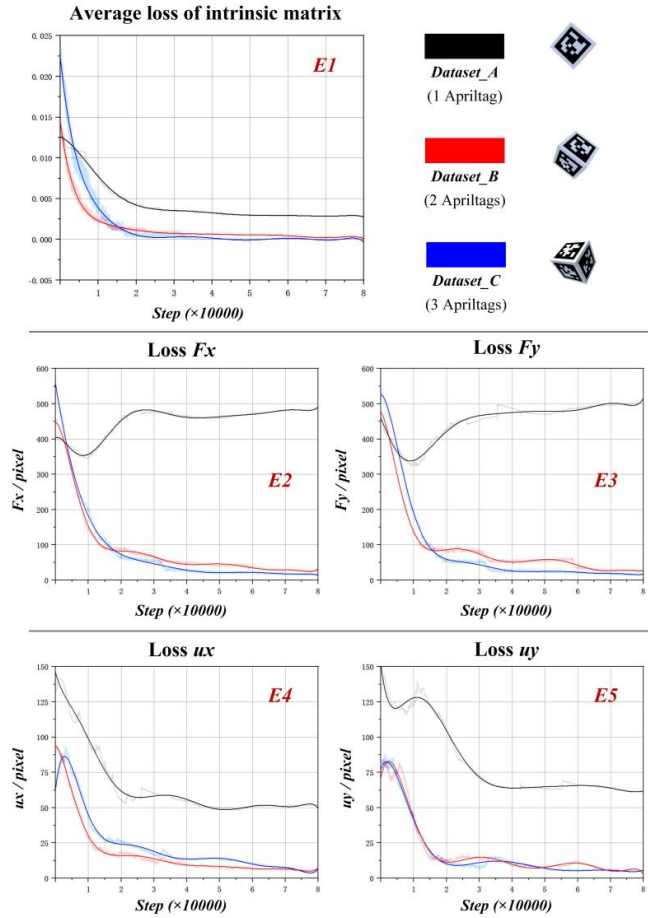


Fig. 10: Comparison results of regressing intrinsic parameters with different number of AprilTag in calibration data. With at least two AprilTags included in the calibration data, we can achieve the expected results. However, when including only one AprilTag, degenerate case is showed up, leading to poor results. Specifically, the black curve in *E1* fails to converge to zero, while the blue and red curves both converge near zero.

curves in *E2* and *E3*,  $F_x$  and  $F_y$  fail to converge, and the losses in *E4* and *E5* exhibit significant deviations from 0. Moreover, Table 2 reveals that the accuracy of the results is significantly inferior to the other two cases.

When the images we used contain more than two AprilTags (*Dataset\_B*, *Dataset\_C*), the estimation can be guaranteed to converge. It can be observed from the quantified data in the table that the parameters trained using the dataset containing three AprilTags achieve higher accuracy, as demonstrated in  $F_x$ ,  $F_y$ ,  $u_x$ , and  $u_y$ . In comparison, the parameters trained with the dataset containing 2 AprilTags converge more rapidly.

In summary, camera intrinsic parameters can be obtained when the Intrinsic Reprojection Loss is trained with dataset containing at least two AprilTags. This demonstrates the effectiveness of the proposed method. If the provided calibration points lie on the same plane, the degenerated case will still occur, resulting in the inability to obtain camera intrinsic parameters. The degenerated case is reproducible in our method.

TABLE 2: Quantitative results of *Exp.2*.

	Train Step	10000	20000	40000	60000	80000
$Loss_{Fx}$	Dataset A	370.06	458.82	460.30	474.59	487.35
	Dataset B	153.53	88.98	53.87	32.47	26.64
	Dataset C	198.08	69.21	26.73	19.41	17.41
$Loss_{Fy}$	Dataset A	343.69	429.86	462.75	470.78	511.29
	Dataset B	144.23	92.43	55.34	32.47	26.64
	Dataset C	197.32	57.01	25.65	21.34	18.91
$Loss_{Ux}$	Dataset A	99.42	62.91	58.71	51.43	51.61
	Dataset B	23.17	15.83	12.85	9.27	7.75
	Dataset C	30.73	19.57	11.37	9.77	7.10
$Loss_{Uy}$	Dataset A	129.51	105.26	64.49	68.22	61.94
	Dataset B	44.52	14.98	13.056	12.48	9.73
	Dataset C	43.17	13.65	14.21	8.31	7.19

#### 4.4 Exp.3 Extrinsic Parameters Estimation

In this experiment, we aim to verify the necessity of extrinsic parameters estimation. While BARF and L2G-NeRF address the joint optimization of NeRF and camera poses, these methods are limited by the initial extrinsic parameters. Specifically, both of the above methods add perturbations to the ground truth extrinsic parameters, leading to camera poses drift, which is then attempted to be rectified during the joint optimization. However, the initial pose of each camera in practical applications still requires huge preparation work, especially for the multi-camera acquisition systems with a large number of cameras. Therefore, in this experiment we randomly provide the initial poses of all cameras and attempt to perform poses estimation on four styles of scenes using the above mentioned two methods. This is done to assess the performance of the previous methods under the condition where no potential poses information is provided.

The results are presented in Fig. 11. The first row illustrates the randomly initialized camera poses of the two methods across the four scenarios, while the second row depicts the stabilized camera poses after training. When the camera poses are initialized randomly, both methods struggle to acquire accurate camera extrinsic parameters. As our proposed method employs the progressive alignment technique introduced by BARF in the joint optimization, it becomes evident that an effective initialization of the camera pose is essential. Further details regarding the convergence process are provided in our supplementary project webpage.

It is worth noting that the camera initialization pose obtained from the calibration cube can satisfy both L2G-NeRF and BARF. The reasons for adopting the BARF approach are as follows: Firstly, as outlined in the original BARF, it makes only minor modifications to the classic Coarse-to-Fine architecture of NeRF, which makes it easily extensible. Secondly, in comparison to L2G-NeRF, these two methods exhibit similar performance under the aforementioned extrinsic initialization conditions. The comparisons are presented in Table 3. Inherited Value refers to the initial poses obtained by calibration cube,  $Loss_R$  and  $Loss_T$  denote the losses associated with the ground truth rotation and translation data. These losses are defined as follows:

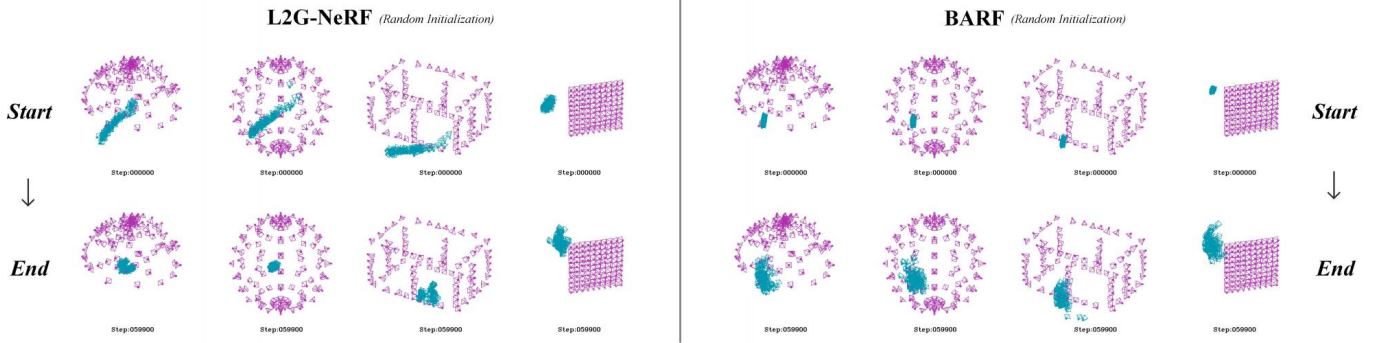


Fig. 11: Comparison of poses estimation performance between BARF and L2G-NeRF with the random initialization poses.

TABLE 3: Comparison of poses estimation performance between BARF and L2G-NeRF with the initialization poses obtained from calibration cube.

Style		Inherited Value	L2G-NeRF	BARF
Ball	$Loss\_R$	0.0392	0.0054	0.0050
	$Loss\_T$	0.1355	0.0463	0.0509
HalfBall	$Loss\_R$	0.0601	0.0183	0.0114
	$Loss\_T$	0.1891	0.0224	0.0321
Room	$Loss\_R$	0.0473	0.0048	0.0027
	$Loss\_T$	0.1844	0.0366	0.0284
Array	$Loss\_R$	0.0561	0.0727	0.0915
	$Loss\_T$	0.2154	0.0149	0.0287

$$\begin{cases} Loss\_R = \sum_{i=0}^n \text{mean}(\|\hat{R}_i - R_i\|_2^2)/n \\ Loss\_T = \sum_{i=0}^n \text{mean}(\|\hat{T}_i - T_i\|_2^2)/n \end{cases} \quad (15)$$

$\hat{R}_i$  and  $R_i$  represent the ground truth and predicted rotation matrices respectively, while  $\hat{T}_i$  and  $T_i$  represent the ground truth and predicted translation matrices.  $\text{mean}()$  represents the mean function.  $n$  represents the total number of poses, which is equal to the number of images in the dataset. It can be observed that when using the initial pose provided by the calibration cube, there is almost no difference in performance between these methods across the four different styles of scenes.

In summary, extrinsic parameter estimation is necessary. Randomly initializing external parameters cannot guarantee obtaining accurate results. By using calibration cube data to initialize extrinsic parameters, we can subsequently achieve precise camera poses using the previously mentioned methods.

#### 4.5 Exp.4 Planar Image Alignment (2D)

In this experiment, we aim to compare the performance of the proposed method with previous works in the task of 2D image alignment. We also explore the performance when calibration points are not provided. We choose the same image "cat" as BARF used from ImageNet[52]. We select five patches sampled from the original image, apply linear transformations and rigid perturbations, and optimize Eq.(13) to find the

transformation  $L$  and  $T$  for each patch. Simultaneously, we train the neural network  $f_{mlp}$  to represent the entire image.

It's important to note that in BARF, MC-NeRF (W/O), and MC-NeRF,  $L$  represents linear transformation, and  $T$  represents rigid rotation and translation. However, in L2G-NeRF, we combine  $L$  and  $T$  and directly replace them with a homography transformation. The reason for this lies in the design of L2G-NeRF, where finding differentiable parameter estimation solvers for custom computational flows is challenging. The homography transformation solver provided by L2G-NeRF itself can simultaneously handle scale, rotation, and translation, and we use the homography transformation to replace  $L$  and  $T$ .

Joint optimization of intrinsic parameters can be equivalent to adding an additional linear transformation  $L$ . To decouple this linear transformation from rotation and translation, we selected six pairs of randomly chosen calibration points as constraints for each patch. This constraint is analogous to the calibration points obtained by calibration cube in 3D dimensional space. In 2D space, the loss function for MC-NeRF is also photometric loss used in NeRF. The final results are shown in Fig.12. In all test models, a 6-layer fully connected network with 256 neurons each is respectively defined. The training epochs are set to 50,000 to ensure convergence for all methods. The training process is demonstrated on our project webpage.

In summary, the inclusion of linear transformations leads to both BARF and L2G-NeRF being unable to produce accurate results. Even in cases where calibration points are not provided, proposed method also faces challenges in achieving precision results. Notably, in the case of MC-NeRF without calibration points, the loss function comprises only the photometric loss and does not include the reprojection term.

#### 4.6 Exp.5 Fix Step VS Global optimization

In this experiment, we aim to validate the effectiveness of the global optimization framework and compare its performance against the Fixed Step NeRF rendering (Intrinsic and extrinsic parameters estimation + NeRF, without other optimization). Fixed Step rendering simulates the typical steps involved in NeRF-based reconstruction using a multi-camera acquisition systems: Initially, camera intrinsic and extrinsic



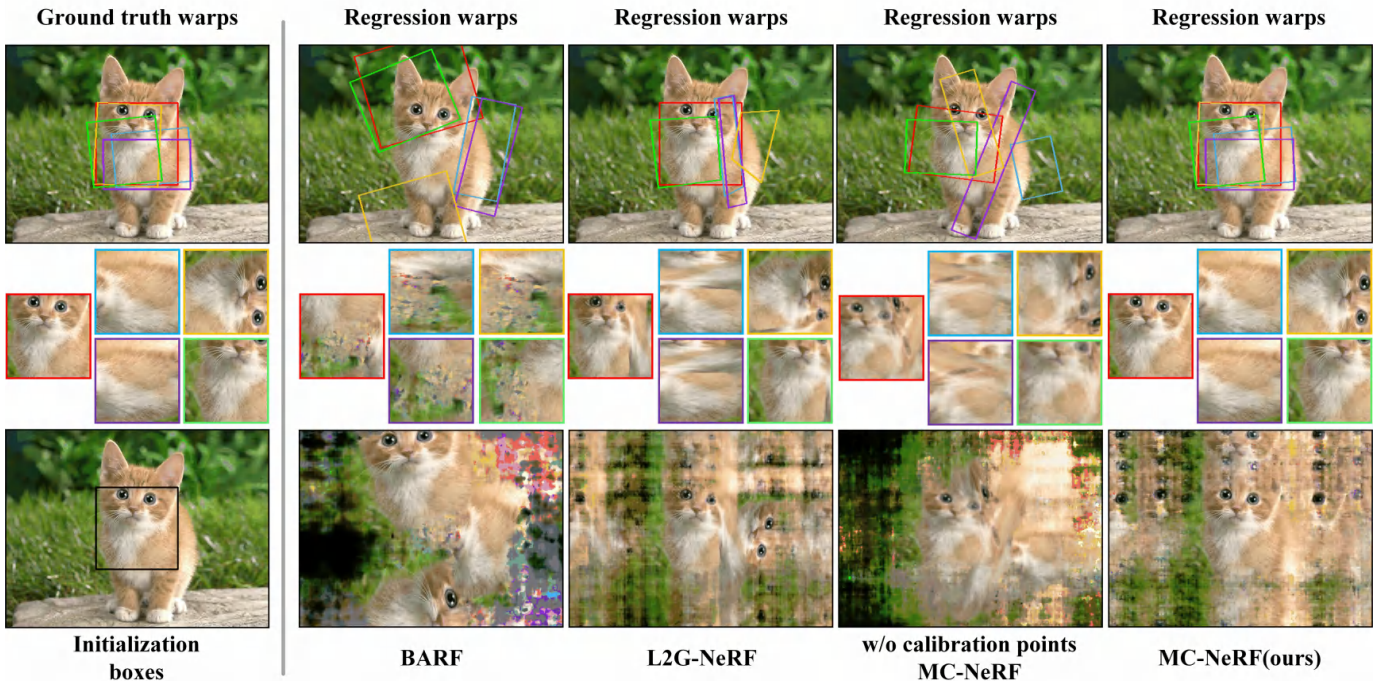


Fig. 12: Qualitative results of the planar image alignment experiment. We visualize the optimized warps (top row), the patch reconstructions in corresponding colors (middle row), and recovered image representation from  $f_{mlp}$  (bottom row). MC-NeRF with calibration points is able to recover accurate alignment and high-fidelity image reconstruction

TABLE 4: Quantitative results of neural image alignment experiment. MC-NeRF optimizes for high-quality alignment and patch reconstruction.

	Corner Error↓ (pixels)	Patch PSNR↑	Patch SSIM↑	Patch LPIPS↓
BARF	85.6157	14.2270	0.5149	0.6641
L2G-NeRF	55.3545	20.5440	0.7884	0.3364
MC-NeRF(w/o)	55.3096	15.9662	0.5923	0.6268
MC-NeRF(ours)	0.4084	40.8309	0.9828	0.0318

parameters are determined using calibration information. Subsequently, NeRF is trained using these fixed parameters to represent the 3D scene. Throughout the NeRF training phase, the camera parameters remain constant.

The experimental results are presented in Fig.13, Table 5, and Table 6. Regarding image rendering quality, in Fig.13, we randomly selected three scenes rendered in four different styles. The global optimization method stands out by producing sharper object boundaries and capturing finer object details. Table 5 shows the average performance for 4 styles, the details across 32 scenes is presented in the supplementary materials. Firstly, MC-NeRF shows a significant performance improvement in Array Style, where it achieves the best scores across all three evaluation metrics. Secondly, we observed that MC-NeRF consistently outperforms in all LPIPS metrics. However, when it comes to PSNR and SSIM, except for the Array scene, MC-NeRF often has lower scores. We explored the reasons, and the detailed analyses and experiments are available in the supplementary materials for further discussion.

Concerning the estimation of camera parameters, as presented in Table 6, global optimization yields more accurate results with a significant improvement. We believe that during the global optimization, NeRF takes the lead as a supervisor for the estimation. To achieve higher-quality rendering results, NeRF enforces the alignment of global rays, and this alignment constraint outperforms traditional camera calibration using calibration points. Additionally, the results also demonstrate that proposed decoupling constraint effectively resolves the coupling issue between intrinsic and extrinsic parameters in joint estimation, allowing for the separation of parameters.

In summary, proposed method is proven to be effective. With global optimization, both the rendering images and the accuracy of estimation parameters surpass those achieved using initial intrinsic and extrinsic parameters. Moreover, in this experiment, we noted that achieving higher-quality rendering results does not necessarily correlate with higher PSNR scores. However, the LPIPS can still objectively reflect rendering performance even in such cases, as demonstrated by the conclusions in Table 5.

#### 4.7 Exp.6 Experiments in real-world dataset

In this experiment, we aim to validate the effectiveness of our method in real-world scenarios. For comparison, we selected commonly used camera parameter estimation methods, including two popular off-the-shelf libraries: COLMAP [5] and MeshRoom [53]. Additionally, we also chose NeRF based methods capable of optimizing camera parameters, including NeRF-- [8] and BARF [10]. Furthermore, we also included

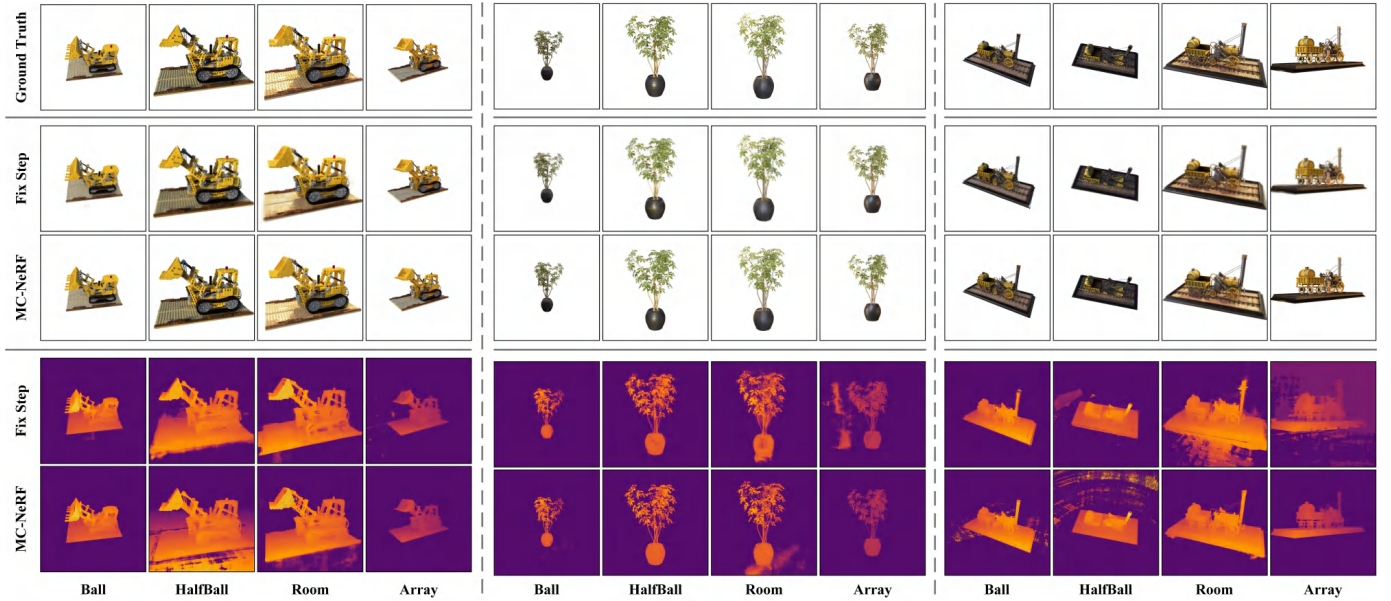


Fig. 13: Rendering results of Fix-Step NeRF and MC-NeRF. We visualize the ground truth images (top row), the rendered RGB images (middle row), and the predicted depth images (bottom row). Thanks to the global optimization, MC-NeRF exhibits improved rendering details and sharper object boundaries.

TABLE 5: Quantitative rendering results of Fix-Step NeRF and MC-NeRF on synthetic datasets.

	Type	PSNR $\uparrow$				SSIM $\uparrow$				LPIPS $\downarrow$			
		Ball	HalfBall	Room	Array	Ball	HalfBall	Room	Array	Ball	HalfBall	Room	Array
Fix-Step	AVE	26.6795	26.4928	24.6243	16.2428	0.9370	0.9222	0.9084	0.8836	0.0717	0.0832	0.1065	0.1662
MC-NeRF	AVE	25.6289	25.1151	25.5698	24.5659	0.9375	0.9072	0.9144	0.9488	0.0473	0.0684	0.0666	0.0406

TABLE 6: Quantitative camera parameters estimation results of Fix-Step NeRF and MC-NeRF on synthetic datasets.

	Type	$Loss_K\downarrow$				$Loss_R\downarrow$				$Loss_T\downarrow$			
		Ball	HalfBall	Room	Array	Ball	HalfBall	Room	Array	Ball	HalfBall	Room	Array
Fix-Step	AVE	10.9625	10.8054	16.6030	27.6182	0.0137	0.0135	0.0313	0.0158	0.0829	0.0813	0.1487	0.2594
MC-NeRF	AVE	3.7384	1.8775	6.8230	4.7167	0.0056	0.0043	0.0100	0.0072	0.0362	0.0263	0.0613	0.0630

the Instant-NGP [35] method. Detailed results can be seen in Fig.14, Table 7.

From Fig.14, it can be seen that compared to other methods, MC-NeRF achieves better rendering quality, an improvement we attribute to addressing the issue of parameter coupling. The middle column of Table 7 shows the estimation results of camera intrinsic parameters by different methods, using mean error to represent performance, with detailed data available in the supplementary material. The right column of Table 7 indicates that MC-NeRF achieved the best results in both PSNR and LPIPS evaluation metrics. It was nearly identical to the top performer in SSIM. In this comparison, we did not provide results for camera extrinsic parameters because methods based on existing off-the-shelf libraries offer only the relative poses of all cameras, and their world coordinate system cannot be modified, making it difficult to align with the ground truth world coordinate system. We believe the rendering results and the estimation performance of camera intrinsic parameters sufficiently demonstrate the effectiveness

of our method.

The results also demonstrate that obtaining more accurate camera parameters can lead to better rendering performance. For the combinations of “Methods + NeRF” and “Methods + BARF”, the camera intrinsics are determined by the “Method” and do not participate in subsequent optimization, avoiding coupling issues. The combination of “Methods + NeRF-” undergoes joint optimization of intrinsics, but it ignores the coupling issue, resulting in lower accuracy in estimating camera intrinsics. Our method addresses the coupling issue, resulting in significant improvements in both rendering quality and the accuracy of intrinsic estimation.

## 5 CONCLUSIONS

In this work, we present Multi-Camera Neural Radiance Fields (MC-NeRF), a 3D representation method designed for multi-camera image acquisition systems, which can joint optimize both camera parameters and NeRF. MC-NeRF breaks the assumption of a unique camera in previous studies and



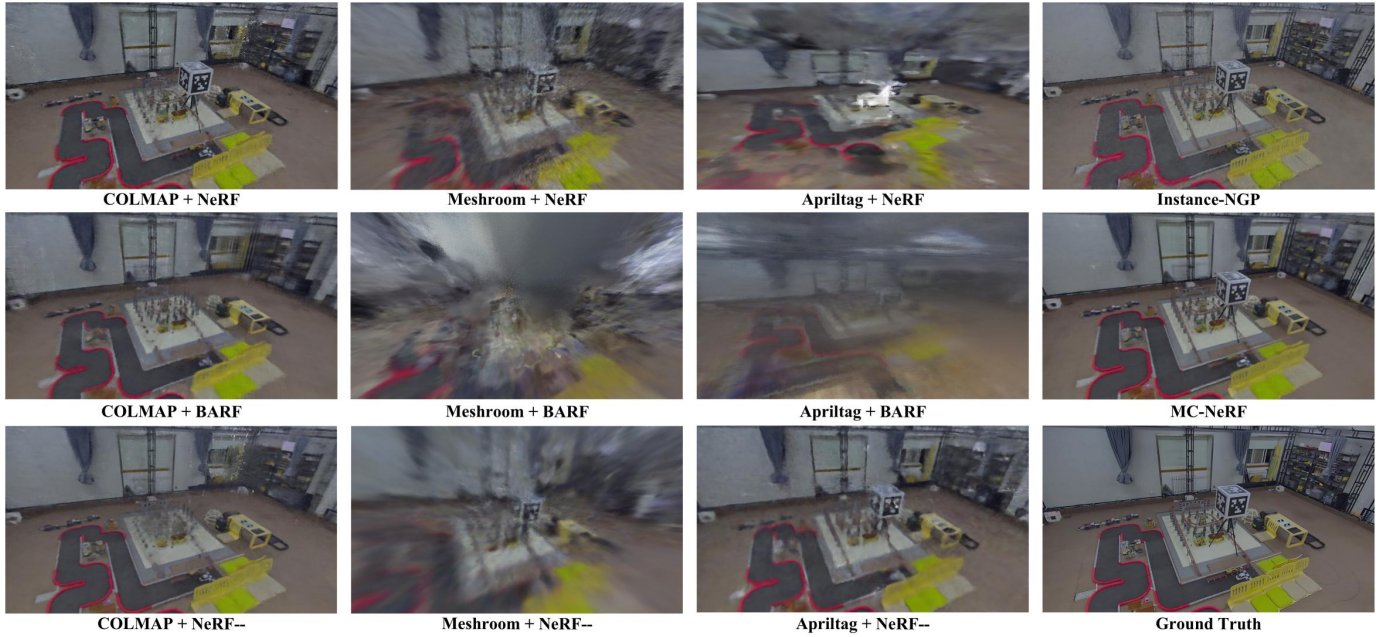


Fig. 14: Rendering results of different methods in real-world dataset. COLMAP, Meshroom, and AprilTag are all used to obtain initial camera parameters. For instance, the item “AprilTag + NeRF—” signifies the process of obtaining camera parameters using AprilTag information from real-world datasets, followed by the reconstruction of the scene using the NeRF— method.

TABLE 7: Quantitative intrinsic parameters estimation results of different methods on real-world datasets.

	Loss_Fx ↓	Loss_Fy ↓	Loss_Ux ↓	Loss_Uy ↓	PSNR ↑	SSIM ↑	LPIPS ↓
COLMAP+NeRF	7.3223	7.3193	12.8605	12.5431	24.0208	0.6935	0.4542
COLMAP+BARF	7.3223	7.3193	12.8605	12.5431	20.8126	0.6342	0.5901
COLMAP+NeRF— —	458.4013	458.4326	15.4003	14.7928	21.3931	0.4192	0.6656
Meshroom+NeRF	375.8785	395.7032	12.8605	12.5431	22.6658	0.6277	0.6395
Meshroom+BARF	375.8785	395.7032	12.8605	12.5431	16.9264	0.5146	0.7792
Meshroom+NeRF— —	665.7271	665.7585	27.7674	23.1451	16.8745	0.5858	0.8135
AprilTag+NeRF	19.4219	19.4130	9.9708	13.8682	23.4455	0.6402	0.5848
AprilTag+BARF	19.4219	19.4130	9.9708	13.8682	17.1713	0.5003	0.8212
AprilTag+NeRF— —	48.7571	48.7466	27.3269	19.8613	22.3521	0.6921	0.5296
Instant-NGP	7.3223	7.3193	12.8605	12.5431	20.8784	0.5978	0.3912
MC-NeRF(ours)	4.2264	4.1906	4.9588	4.0681	24.3339	0.6923	0.3589

avoids providing initialized camera parameters. We analyzed the challenges of joint optimization, including coupling issue and intrinsics degenerated case. Based on this analysis, we design the framework with training sequence, calibration objects, and a calibration data acquisition strategy. Furthermore, we also provide a datasets with each image corresponding to different camera parameters, including both virtual and real-world scenes. The proposed method primarily tackles the substantial workload associated with acquiring multi-camera intrinsic and extrinsic parameters when employing multi-camera acquisition systems for 3D scene representation. Experiments demonstrate that proposed method achieves better rendering results and more accurate camera parameters. Code

and models will be made available to the research community to facilitate reproducible research.

## ACKNOWLEDGMENTS

This work is partly supported by National Natural Science Foundation of China (Grant No. 62233002, 61973034, U1913203 and CJSP Q2018229). The authors would like to thank Tianji Jiang, Xi Xu, Jiadong Tang, Zhaoxiang Liang, Xihan Wang, Dianyi Yang, and all other members of the ININ Lab of the Beijing Institute of Technology for their contribution to this work.



## References

- [1] B. Mildenhall, P. P. Srinivasan, M. Tancik, J. T. Barron, R. Ramamoorthi, and R. Ng, “Nerf: Representing scenes as neural radiance fields for view synthesis,” in *Computer Vision – ECCV 2020*, A. Vedaldi, H. Bischof, T. Brox, and J.-M. Frahm, Eds., Springer International Publishing, 2020, pp. 405–421.
- [2] B. Mildenhall, P. P. Srinivasan, R. Ortiz-Cayon, *et al.*, “Local light field fusion: Practical view synthesis with prescriptive sampling guidelines,” *ACM Trans. Graph.*, vol. 38, no. 4, 2019.
- [3] L. Liu, J. Gu, K. Z. Lin, T.-S. Chua, and C. Theobalt, “Neural sparse voxel fields,” in *Proceedings of the 34th International Conference on Neural Information Processing Systems*, ser. NIPS’20, Vancouver, BC, Canada: Curran Associates Inc, 2020.
- [4] J. T. Barron, B. Mildenhall, D. Verbin, P. P. Srinivasan, and P. Hedman, “Mip-nerf 360: Unbounded anti-aliased neural radiance fields,” in *2022 IEEE/CVF Conference on Computer Vision and Pattern Recognition (CVPR)*, 2022, pp. 5460–5469.
- [5] J. L. Schönberger and J.-M. Frahm, “Structure-from-motion revisited,” in *2016 IEEE Conference on Computer Vision and Pattern Recognition (CVPR)*, 2016, pp. 4104–4113.
- [6] K. Park, P. Henzler, B. Mildenhall, J. T. Barron, and R. Martin-Brualla, “Camp: Camera preconditioning for neural radiance fields,” *ACM Trans. Graph.*, vol. 42, no. 6, 2023.
- [7] Y. Jeong, S. Ahn, C. B. Choy, A. Anandkumar, M. Cho, and J. Park, “Self-calibrating neural radiance fields,” *2021 IEEE/CVF International Conference on Computer Vision (ICCV)*, pp. 5826–5834, 2021.
- [8] Z. Wang, S. Wu, W. Xie, M. Chen, and V. A. Prisacariu, *Nerf-: Neural radiance fields without known camera parameters*, 2022. arXiv: 2102.07064 [cs.CV].
- [9] Y. Chen, X. Chen, X. Wang, *et al.*, “Local-to-global registration for bundle-adjusting neural radiance fields,” in *Proceedings of the IEEE/CVF Conference on Computer Vision and Pattern Recognition*, 2023, pp. 8264–8273.
- [10] C.-H. Lin, W.-C. Ma, A. Torralba, and S. Lucey, “Barf: Bundle-adjusting neural radiance fields,” in *2021 IEEE/CVF International Conference on Computer Vision (ICCV)*, 2021, pp. 5721–5731.
- [11] O. Faugeras, *Three-dimensional computer vision: a geometric viewpoint*. MIT press, 1993.
- [12] R. Tsai, “A versatile camera calibration technique for high-accuracy 3d machine vision metrology using off-the-shelf tv cameras and lenses,” *IEEE Journal on Robotics and Automation*, vol. 3, no. 4, pp. 323–344, 1987.
- [13] Z. Zhang, “Flexible camera calibration by viewing a plane from unknown orientations,” in *Proceedings of the Seventh IEEE International Conference on Computer Vision*, vol. 1, 1999, 666–673 vol.1.
- [14] H. Lee, E. Shechtman, J. Wang, and S. Lee, “Automatic upright adjustment of photographs with robust camera calibration,” *IEEE Transactions on Pattern Analysis and Machine Intelligence*, vol. 36, no. 5, pp. 833–844, 2014.
- [15] M. Zhai, S. Workman, and N. Jacobs, “Detecting vanishing points using global image context in a non-manhattanworld,” in *2016 IEEE Conference on Computer Vision and Pattern Recognition (CVPR)*, 2016, pp. 5657–5665.
- [16] Q. Chen, H. Wu, and T. Wada, “Camera calibration with two arbitrary coplanar circles,” in *Computer Vision - ECCV 2004*, T. Pajdla and J. Matas, Eds., Springer Berlin Heidelberg, 2004, pp. 521–532.
- [17] O. Bogdan, V. Eckstein, F. Rameau, and J.-C. Bazin, “Deepcalib: A deep learning approach for automatic intrinsic calibration of wide field-of-view cameras,” in *Proceedings of the 15th ACM SIGGRAPH European Conference on Visual Media Production*, New York, NY, USA: Association for Computing Machinery, 2018.
- [18] Y. Hold-Geoffroy, D. Piché-Meunier, K. Sunkavalli, J.-C. Bazin, F. Rameau, and J.-F. Lalonde, “A perceptual measure for deep single image camera and lens calibration,” *IEEE Transactions on Pattern Analysis and Machine Intelligence*, vol. 45, no. 9, pp. 10 603–10 614, 2023.
- [19] M. Landy and J. A. Movshon, “Shape from x: Psychophysics and computation,” in *Computational Models of Visual Processing*. 1991, pp. 305–330.
- [20] M. Goesele, N. Snavely, B. Curless, H. Hoppe, and S. Seitz, “Multi-view stereo for community photo collections,” 2007, pp. 1–8.
- [21] C. M. Parameshwara, G. Hari, C. Fermüller, N. J. Sanket, and Y. Aloimonos, “Diffposenet: Direct differentiable camera pose estimation,” in *2022 IEEE/CVF Conference on Computer Vision and Pattern Recognition (CVPR)*, 2022, pp. 6835–6844.
- [22] S. Lee and Y.-K. Moon, “Camera pose estimation using voxel-based features for autonomous vehicle localization tracking,” in *2022 37th International Technical Conference on Circuits/Systems, Computers and Communications (ITC-CSCC)*, 2022, pp. 185–188.
- [23] W. Ye, X. Lan, S. Chen, *et al.*, “Pvo: Panoptic visual odometry,” in *2023 IEEE/CVF Conference on Computer Vision and Pattern Recognition (CVPR)*, IEEE Computer Society, 2023, pp. 9579–9589.
- [24] C.-C. Chiu, H.-K. Yang, H.-W. Chen, Y.-W. Chen, and C.-Y. Lee, “Vitvo: Vision transformer based visual odometry with attention supervision,” in *2023 18th International Conference on Machine Vision and Applications (MVA)*, IEEE, 2023, pp. 1–5.
- [25] A. Kendall, M. Grimes, and R. Cipolla, “Posenet: A convolutional network for real-time 6-dof camera relocalization,” in *2015 IEEE International Conference on Computer Vision (ICCV)*, IEEE Computer Society, 2015, pp. 2938–2946.
- [26] Y.-Y. Jau, R. Zhu, H. Su, and M. Chandraker, “Deep keypoint-based camera pose estimation with geometric constraints,” in *2020 IEEE/RSJ International Conference on Intelligent Robots and Systems (IROS)*, 2020, pp. 4950–4957.

- [27] L. Yen-Chen, P. Florence, J. T. Barron, A. Rodriguez, P. Isola, and T.-Y. Lin, “Inerf: Inverting neural radiance fields for pose estimation,” in *2021 IEEE/RSJ International Conference on Intelligent Robots and Systems (IROS)*, IEEE Press, 2021, pp. 1323–1330.
- [28] K. Zhang, G. Riegler, N. Snavely, and V. Koltun, *Nerf++: Analyzing and improving neural radiance fields*, 2020. arXiv: 2010.07492.
- [29] R. Martin-Brualla, N. Radwan, M. M. Sajjadi, J. T. Barron, A. Dosovitskiy, and D. Duckworth, “Nerf in the wild: Neural radiance fields for unconstrained photo collections,” in *2021 IEEE/CVF Conference on Computer Vision and Pattern Recognition (CVPR)*, IEEE Computer Society, 2021, pp. 7206–7215.
- [30] K. Schwarz, Y. Liao, M. Niemeyer, and A. Geiger, “Graf: Generative radiance fields for 3d-aware image synthesis,” in *Proceedings of the 34th International Conference on Neural Information Processing Systems*, Curran Associates Inc., 2020.
- [31] J. T. Barron, B. Mildenhall, M. Tancik, P. Hedman, R. Martin-Brualla, and P. P. Srinivasan, “Mip-nerf: A multiscale representation for anti-aliasing neural radiance fields,” in *2021 IEEE/CVF International Conference on Computer Vision (ICCV)*, 2021, pp. 5835–5844.
- [32] H. Jin, I. Liu, P. Xu, *et al.*, “Tensor: Tensorial inverse rendering,” in *2023 IEEE/CVF Conference on Computer Vision and Pattern Recognition (CVPR)*, IEEE Computer Society, 2023, pp. 165–174.
- [33] T. Hu, S. Liu, Y. Chen, T. Shen, and J. Jia, “Efficientnerf - efficient neural radiance fields,” in *2022 IEEE/CVF Conference on Computer Vision and Pattern Recognition (CVPR)*, 2022, pp. 12 892–12 901.
- [34] J. T. Barron, B. Mildenhall, D. Verbin, P. P. Srinivasan, and P. Hedman, “Zip-nerf: Anti-aliased grid-based neural radiance fields,” in *2023 IEEE/CVF International Conference on Computer Vision (ICCV)*, IEEE Computer Society, 2023, pp. 19 640–19 648.
- [35] T. Müller, A. Evans, C. Schied, and A. Keller, “Instant neural graphics primitives with a multiresolution hash encoding,” *ACM Trans. Graph.*, vol. 41, no. 4, pp. 102:1–102:15, Jul. 2022.
- [36] A. Chen, Z. Xu, A. Geiger, J. Yu, and H. Su, “Tensorf: Tensorial radiance fields,” in *Computer Vision – ECCV 2022: 17th European Conference, Tel Aviv, Israel, October 23–27, 2022, Proceedings, Part XXXII*, Springer-Verlag, 2022, pp. 333–350.
- [37] C. Wu, “Towards linear-time incremental structure from motion,” in *2013 International Conference on 3D Vision - 3DV 2013*, 2013, pp. 127–134.
- [38] F. Radenovic, J. L. Schönberger, D. Ji, J.-M. Frahm, O. Chum, and J. Matas, “From dusk till dawn: Modeling in the dark,” in *2016 IEEE Conference on Computer Vision and Pattern Recognition (CVPR)*, 2016, pp. 5488–5496.
- [39] Z. Li, S. Niklaus, N. Snavely, and O. Wang, “Neural scene flow fields for space-time view synthesis of dynamic scenes,” in *2021 IEEE/CVF Conference on Computer Vision and Pattern Recognition (CVPR)*, 2021, pp. 6494–6504.
- [40] S.-F. Chng, S. Ramasinghe, J. Sherrah, and S. Lucey, “Gaussian activated neural radiance fields for high fidelity reconstruction and pose estimation,” in *Computer Vision – ECCV 2022*, S. Avidan, G. Brostow, M. Cissé, G. M. Farinella, and T. Hassner, Eds., Springer Nature Switzerland, 2022, pp. 264–280.
- [41] Y. Xia, H. Tang, R. Timofte, and L. V. Gool, “Sinerf: Sinusoidal neural radiance fields for joint pose estimation and scene reconstruction,” in *British Machine Vision Conference*, 2022.
- [42] K. Park, U. Sinha, J. T. Barron, *et al.*, “Nerfies: Deformable neural radiance fields,” in *2021 IEEE/CVF International Conference on Computer Vision (ICCV)*, 2021, pp. 5845–5854.
- [43] A. Hertz, O. Perel, R. Giryes, O. Sorkine-Hornung, and D. Cohen-Or, “Sape: Spatially-adaptive progressive encoding for neural optimization,” in *Neural Information Processing Systems*, 2021.
- [44] A. Vaswani, N. Shazeer, N. Parmar, *et al.*, “Attention is all you need,” in *Advances in Neural Information Processing Systems*, I. Guyon, U. V. Luxburg, S. Bengio, *et al.*, Eds., vol. 30, Curran Associates, Inc., 2017.
- [45] W. Bian, Z. Wang, K. Li, and J. Bian, “Nope-nerf: Optimising neural radiance field with no pose prior,” in *2023 IEEE/CVF Conference on Computer Vision and Pattern Recognition (CVPR)*, IEEE Computer Society, 2023, pp. 4160–4169.
- [46] P. Truong, M. Rakotosaona, F. Manhardt, and F. Tombari, “Sparf: Neural radiance fields from sparse and noisy poses,” in *2023 IEEE/CVF Conference on Computer Vision and Pattern Recognition (CVPR)*, IEEE Computer Society, 2023, pp. 4190–4200.
- [47] Y. Chen and G. Lee, “Dbarf: Deep bundle-adjusting generalizable neural radiance fields,” in *2023 IEEE/CVF Conference on Computer Vision and Pattern Recognition (CVPR)*, IEEE Computer Society, 2023, pp. 24–34.
- [48] Q. Wang, Z. Wang, K. Genova, *et al.*, “Ibrnet: Learning multi-view image-based rendering,” in *2021 IEEE/CVF Conference on Computer Vision and Pattern Recognition (CVPR)*, IEEE Computer Society, 2021, pp. 4688–4697.
- [49] A. Yu, V. Ye, M. Tancik, and A. Kanazawa, “Pixelnerf: Neural radiance fields from one or few images,” in *2021 IEEE/CVF Conference on Computer Vision and Pattern Recognition (CVPR)*, 2021, pp. 4576–4585.
- [50] Q. Meng, A. Chen, H. Luo, *et al.*, “Gnerf: Gan-based neural radiance field without posed camera,” in *2021 IEEE/CVF International Conference on Computer Vision (ICCV)*, 2021, pp. 6331–6341.
- [51] R. I. Hartley and A. Zisserman, *Multiple View Geometry in Computer Vision*, 2nd ed. Cambridge University Press, 2003, ISBN: 0521540518.
- [52] J. Deng, W. Dong, R. Socher, L.-J. Li, K. Li, and L. Fei-Fei, “Imagenet: A large-scale hierarchical image database,” in *2009 IEEE Conference on Computer Vision and Pattern Recognition*, 2009, pp. 248–255. DOI: 10.1109/CVPR.2009.5206848.

- [53] C. Griwodz, S. Gasparini, L. Calvet, *et al.*, “Alice-vision Meshroom: An open-source 3D reconstruction pipeline,” in *Proceedings of the 12th ACM Multimedia Systems Conference - MMSys '21*, ACM Press, 2021.

## Supplementary Materials

### *Detail performance in Synthetic Datasets*

In the Synthetic datasets we have released, a total of 32 scenes are included. Table 8 and Table 9 show the comparative results between MC-NeRF and Fix-Step under each scene. In the original manuscript, the aforementioned results correspond to Tables 6 and 7.

### *Supplementary Experiment A: Stacking Techniques*

In MC-NeRF, the NeRF component does not undergo significant modifications, the method for estimating camera parameters is derived from NeRF— and BARF. However, simply stacking methods cannot achieve the effect of MC-NeRF, mainly for two reasons: First, the parameter coupling issue, which has already been emphasized in the original manuscript. For this part, we provide additional AprilTag information to ensure the parameters can be decoupled. Second, the training process needs to follow the training sequence diagram proposed in the manuscript (Fig. 8: Training Sequential Diagram). Here, we conducted comparative experiments by simply stacking the techniques of BARF and NeRF— and using the same camera parameter initialization process as MC-NeRF. The results under 32 scenes are shown in Fig.15 and Table 10.

As shown in Table 10, Mix-Step represents the hybrid method of *AprilTag + BARF + NeRF—*, and the comparative results demonstrate that simply stacking techniques without adhering to the aforementioned conditions cannot achieve the desired effect. This further validates the effectiveness of our proposed method.

### *Supplementary Experiment B: NeRF with Off-the-Shelf Libraries*

In addition to the comparison experiments with synthetic datasets described in the original manuscript, we carried out further supplementary experiments to substantiate the performance of MC-NeRF. In these experiments, we employed camera parameters obtained using SFM (Structure from Motion) techniques from well-established libraries including COLMAP and Meshroom. These parameters are then used to train with NeRF. The count of usable images sourced from these libraries is presented in Table 11.

Table 11 demonstrates that with synthetic datasets, SFM-based methods exhibit unreliable performance, leading to a significant loss of image data. This can be attributed to the simplistic background textures prevalent in synthetic data, coupled with the inherently limited number of images available. Conversely, the estimation method using AprilTag does not encounter these issues, which is one of the reasons we opted for this method.

To ensure that the experimental results are meaningful, we restricted our training to scenes with more than 30 usable images. The rendering results illustrated in Fig. 16 and Table 12. From Fig. 16, it is seen that MC-NeRF achieves better



TABLE 8: Quantitative rendering results of Fix-Step NeRF and MC-NeRF on all scenes.

	Scene	PSNR $\uparrow$				SSIM $\uparrow$				LPIPS $\downarrow$			
		Ball	HalfBall	Room	Array	Ball	HalfBall	Room	Array	Ball	HalfBall	Room	Array
Fix-Step	Computer	25.1685	25.3800	20.6838	16.6674	0.9230	0.9088	0.8869	0.8838	0.0882	0.1020	0.1419	0.1571
	Ficus	26.9503	25.9101	25.3156	17.2587	0.9539	0.9427	0.9313	0.8893	0.0431	0.0542	0.0762	0.1590
	Gate	28.9521	28.9134	29.8277	18.1242	0.9416	0.9348	0.9341	0.8853	0.0542	0.0633	0.0782	0.1515
	Lego	25.5330	25.1424	24.9465	15.6066	0.9219	0.8822	0.8742	0.8672	0.0998	0.1106	0.1214	0.1897
	Materials	26.7998	25.8398	25.8738	16.3879	0.9443	0.9504	0.9462	0.8953	0.0666	0.0543	0.0634	0.1618
	Snowtruck	25.1714	25.1153	23.7291	14.7770	0.9166	0.9114	0.8989	0.8770	0.0959	0.1093	0.1287	0.1728
	Statue	30.5160	31.5379	24.4189	16.0766	0.9710	0.9694	0.9380	0.8938	0.0383	0.0420	0.0954	0.1571
	Train	24.3452	24.1038	22.1991	15.0438	0.9240	0.8779	0.8578	0.8768	0.0876	0.1301	0.1466	0.1807
	Mean	26.6795	26.4928	24.6243	16.2428	0.9370	0.9222	0.9084	0.8836	0.0717	0.0832	0.1065	0.1662
MC-NeRF	Computer	24.2311	23.0962	23.6603	24.6946	0.9217	0.8876	0.9008	0.9395	0.0794	0.0933	0.1004	0.0444
	Ficus	24.9479	24.7662	26.5778	24.2929	0.9488	0.9070	0.9386	0.9504	0.0336	0.0519	0.0449	0.0387
	Gate	27.9102	26.0876	29.3081	26.7734	0.9333	0.9131	0.9250	0.9356	0.0519	0.0525	0.0602	0.0439
	Lego	24.1226	23.4818	23.3858	24.3502	0.9227	0.8682	0.8837	0.9629	0.0620	0.0901	0.0874	0.0343
	Materials	26.8742	26.6170	27.1323	25.0106	0.9484	0.9488	0.9529	0.9601	0.0321	0.0423	0.0294	0.0397
	Snowtruck	24.8742	24.0678	23.4415	23.3363	0.9211	0.8882	0.8937	0.9375	0.0433	0.0882	0.0874	0.0451
	Statue	28.6882	29.2767	28.7953	24.6619	0.9731	0.9670	0.9612	0.9651	0.0303	0.0301	0.0398	0.0281
	Train	23.3830	23.5271	22.2576	23.4073	0.9311	0.8773	0.8589	0.9395	0.0454	0.0991	0.0835	0.0507
	Mean	25.6289	25.1151	25.5698	24.5659	0.9375	0.9072	0.9144	0.9488	0.0473	0.0684	0.0666	0.0406

rendering details, particularly in terms of object edge delineation. Furthermore, in quantitative results, MC-NeRF also outperforms the other two methods across all three metrics.

To ensure the meaningfulness of the experimental results, we limited our training to scenes with more than 30 usable images. The results are illustrated in Fig. 16 and detailed in Table 12. Fig. 16 demonstrates that MC-NeRF provides superior rendering details, especially in object edge delineation. Moreover, MC-NeRF outperforms the other two methods in quantitative evaluations across all three metrics.

### Supplementary Experiment C: PSNR and SSIM evaluation metrics analysis

Although MC-NeRF achieved better rendering details, it scored lower on both PSNR and SSIM evaluation metrics. We believe this is related to the alignment of object boundaries, and the reason behind this phenomenon is the absence of enforced ray alignment constraints for rendering in MC-NeRF. Specifically, the camera parameters of Fix-Step NeRF are constant and remain stable during the rendering stage, which maintains a fixed ray distribution, and all fitting computations contained within NeRF’s MLPs. It can be observed that to compensate for the ray distribution error resulting from inaccuracies in camera parameters, the rendered objects exhibit a multi-layer shadow structure. In Fig.17, the boundaries of the computer show noticeable shadows, while those of MC-NeRF appear much clearer and sharper. This multi-layer shadow structure has more advantages for pixel-to-pixel calculation methods like PSNR. If the clear-edged object generated by MC-NeRF is not aligned with the ground truth, the PSNR scores can be easily affected by the background, resulting in lower scores. Although MC-NeRF has some drawbacks in terms of boundary alignment, we prioritize high-quality

rendering. Additionally, based on the rendering images, we believe that this alignment error is tolerable and unlikely to be readily noticeable.

Moreover, in this experiment, we noted that achieving higher-quality rendering results does not necessarily correlate with higher PSNR and SSIM scores. Because even when the estimation results for both intrinsic and extrinsic parameters are highly accurate, their values are often challenging to align perfectly with ground truth. This leads to slight shifts of objects in the rendered image, which have a notable impact when calculating pixel-wise differences for PSNR and SSIM. However, the LPIPS can still objectively reflect rendering performance even in such cases.

TABLE 9: Camera parameters estimation results of Fix-Step NeRF and MC-NeRF on all scenes.

	Scene	$Loss_K \downarrow$				$Loss_R \downarrow$				$Loss_T \downarrow$			
		Ball	HalfBall	Room	Array	Ball	HalfBall	Room	Array	Ball	HalfBall	Room	Array
Fix-Step	Computer	12.0723	11.2606	17.6997	28.6428	0.0131	0.0124	0.0309	0.0157	0.0806	0.0830	0.1530	0.2616
	Ficus	10.2547	11.0173	16.9588	28.9794	0.0147	0.0128	0.0276	0.0148	0.0802	0.0925	0.1507	0.2714
	Gate	10.0650	11.0287	17.4918	26.3233	0.0134	0.0138	0.0344	0.0157	0.0781	0.0797	0.1604	0.2433
	Lego	10.3323	11.0146	17.0964	24.9460	0.0135	0.0163	0.0315	0.0156	0.0787	0.0830	0.1577	0.2505
	Materials	11.3069	10.8165	15.3205	27.4074	0.0157	0.0148	0.0300	0.0193	0.1005	0.0860	0.1458	0.2704
	Snowtruck	11.7263	10.9522	13.9390	29.3079	0.0131	0.0136	0.0270	0.0141	0.0811	0.0727	0.1106	0.2619
	Statue	10.3607	10.0933	17.1346	27.5365	0.0123	0.0104	0.0352	0.0149	0.0775	0.0774	0.1480	0.2569
	Train	11.5821	10.2598	17.1833	27.8020	0.0136	0.0139	0.0334	0.0164	0.0862	0.0762	0.1630	0.2595
	Mean	10.9625	10.8054	16.6030	27.6182	0.0137	0.0135	0.0313	0.0158	0.0829	0.0813	0.1487	0.2594
MC-NeRF	Computer	1.2758	5.4864	6.3094	5.0589	0.0033	0.0101	0.0090	0.0057	0.0231	0.0398	0.0696	0.0549
	Ficus	1.2524	1.3501	3.0402	5.6844	0.0031	0.0042	0.0036	0.0081	0.0209	0.0234	0.0306	0.0734
	Gate	11.9388	1.2863	5.4361	4.6863	0.0089	0.0043	0.0066	0.0064	0.0426	0.0607	0.0511	0.0524
	Lego	1.1857	1.5403	5.6895	5.1950	0.0024	0.0032	0.0073	0.0073	0.0243	0.0243	0.0546	0.0661
	Materials	4.0039	1.5266	9.3145	4.1782	0.0043	0.0035	0.0151	0.0088	0.0398	0.0177	0.1096	0.0709
	Snowtruck	1.5929	1.2136	8.6714	4.2423	0.0036	0.0032	0.0209	0.0058	0.0267	0.0156	0.0659	0.0619
	Statue	1.2508	1.2926	5.1592	4.2392	0.0040	0.0032	0.0073	0.0082	0.0184	0.0148	0.0539	0.0654
	Train	7.4066	1.3244	10.9638	4.4496	0.0151	0.0030	0.0101	0.0069	0.0940	0.0139	0.0549	0.0588
	Mean	3.7384	1.8775	6.8230	4.7167	0.0056	0.0043	0.0100	0.0072	0.0362	0.0263	0.0613	0.0630

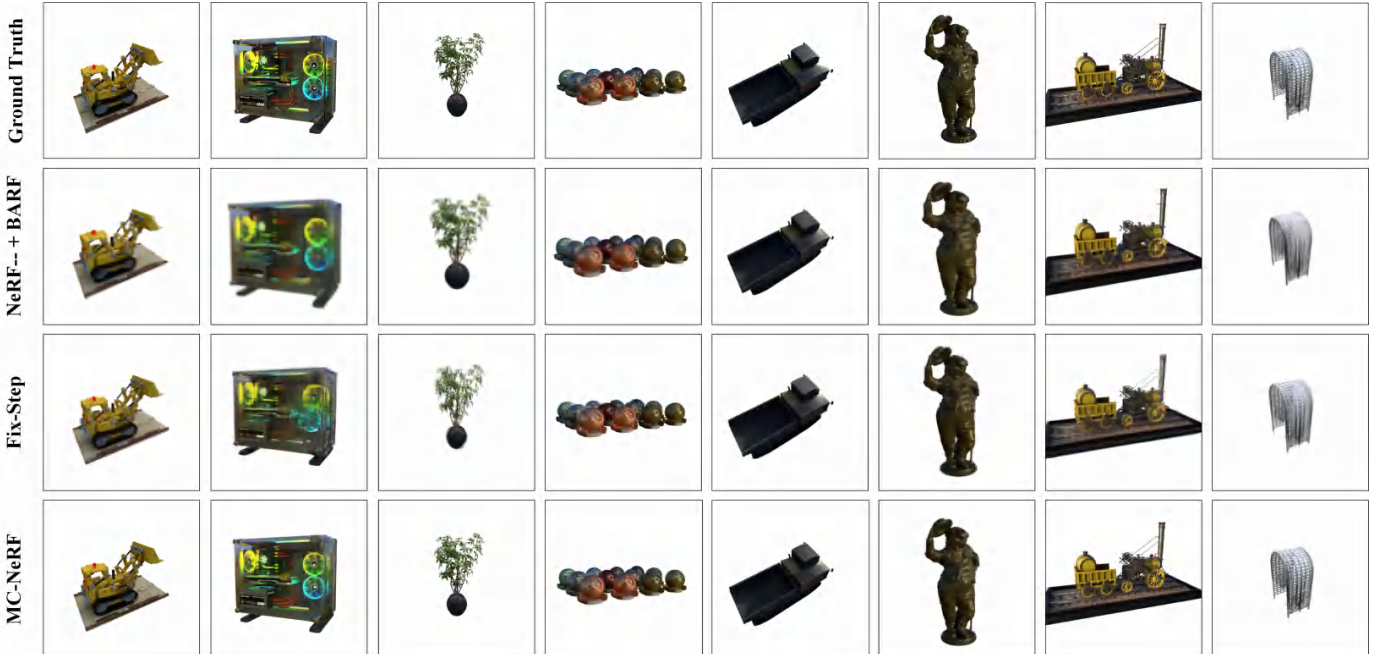


Fig. 15: Rendering results of BARF+NeRF—, Fix-Step NeRF and MC-NeRF. The first row represents the ground truth images, while the remaining rows display rendering results.

TABLE 10: Quantitative rendering results of Mix-Step and MC-NeRF on all scenes.

	Scene	PSNR $\uparrow$				SSIM $\uparrow$				LPIPS $\downarrow$			
		Ball	HalfBall	Room	Array	Ball	HalfBall	Room	Array	Ball	HalfBall	Room	Array
Mix-Step	Computer	15.6289	14.1684	18.0732	22.0304	0.7937	0.8445	0.7438	0.9172	0.2376	0.2686	0.3228	0.0634
	Ficus	17.4136	16.2707	21.0218	20.4416	0.9231	0.8959	0.9263	0.9479	0.1302	0.1752	0.1551	0.0941
	Gate	19.0948	18.1299	23.5322	21.3187	0.9185	0.7781	0.9234	0.9358	0.1509	0.1874	0.1775	0.1045
	Lego	20.7237	18.6574	21.0971	17.9275	0.8615	0.7870	0.7564	0.9099	0.1389	0.3503	0.2937	0.1658
	Materials	18.6585	16.9294	24.4285	20.4265	0.9118	0.8764	0.9234	0.9531	0.1068	0.1386	0.0976	0.0753
	Snowtruck	19.3878	20.0831	21.3667	16.7986	0.8891	0.9184	0.8259	0.9192	0.1417	0.0917	0.2615	0.1216
	Statue	17.9503	19.1121	23.1452	17.5167	0.9231	0.8923	0.8876	0.9539	0.1161	0.1999	0.1767	0.0827
	Train	18.6715	18.6559	18.8509	21.3719	0.8464	0.8810	0.9172	0.9175	0.1729	0.0966	0.2571	0.0875
	Mean	18.4411	17.7508	21.4395	19.7290	0.8834	0.8592	0.8437	0.9318	0.1494	0.1885	0.2178	0.0994
MC-NeRF	Computer	24.2311	23.0962	23.6603	24.6946	0.9217	0.8876	0.9008	0.9395	0.0794	0.0933	0.1004	0.0444
	Ficus	24.9479	24.7662	26.5778	24.2929	0.9488	0.9070	0.9386	0.9504	0.0336	0.0519	0.0449	0.0387
	Gate	27.9102	26.0876	29.3081	26.7734	0.9333	0.9131	0.9250	0.9356	0.0519	0.0525	0.0602	0.0439
	Lego	24.1226	23.4818	23.3858	24.3502	0.9227	0.8682	0.8837	0.9629	0.0620	0.0901	0.0874	0.0343
	Materials	26.8742	26.6170	27.1323	25.0106	0.9484	0.9488	0.9529	0.9601	0.0321	0.0423	0.0294	0.0397
	Snowtruck	24.8742	24.0678	23.4415	23.3363	0.9211	0.8882	0.8937	0.9375	0.0433	0.0882	0.0874	0.0451
	Statue	28.6882	29.2767	28.7953	24.6619	0.9731	0.9670	0.9612	0.9651	0.0303	0.0301	0.0398	0.0281
	Train	23.3830	23.5271	22.2576	23.4073	0.9311	0.8773	0.8589	0.9395	0.0454	0.0991	0.0835	0.0507
	Mean	25.6289	25.1151	25.5698	24.5659	0.9375	0.9072	0.9144	0.9488	0.0473	0.0684	0.0666	0.0406

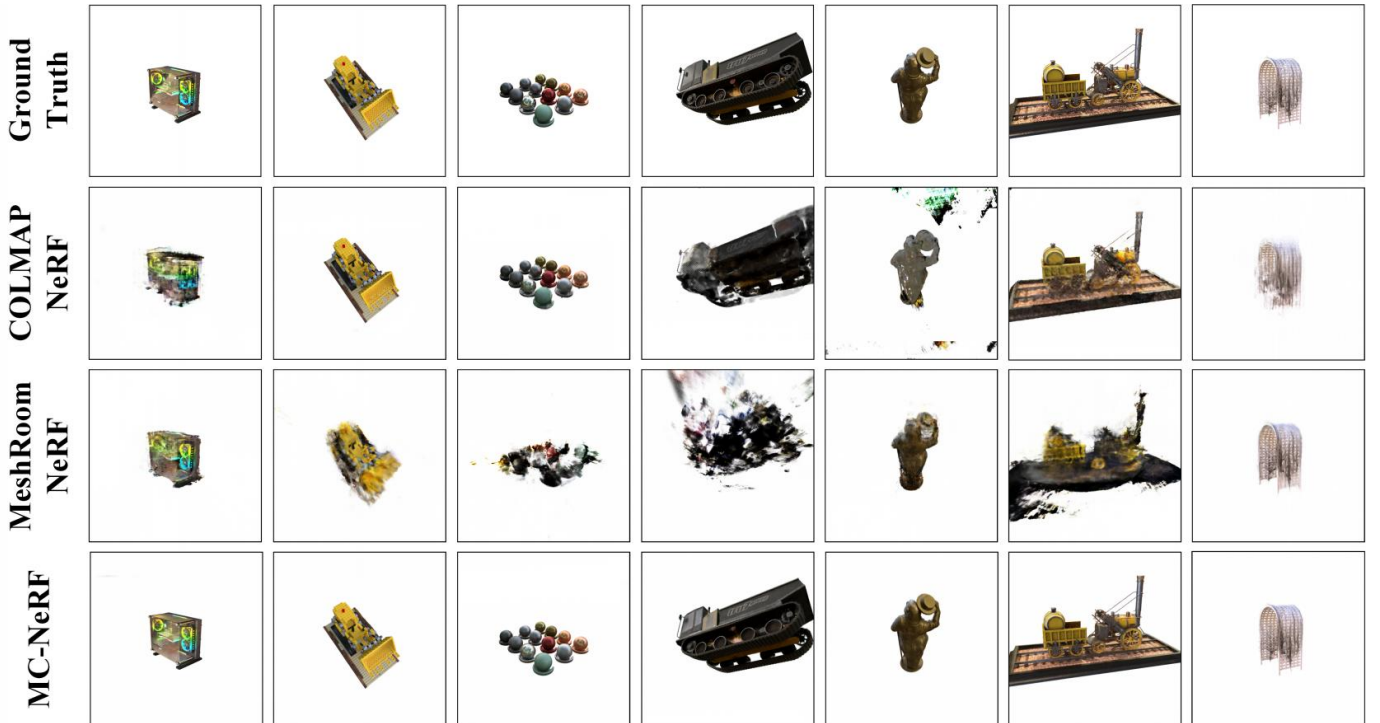


Fig. 16: Rendering results of COLMAP+NeRF, Meshroom+NeRF and MC-NeRF. The first row represents the ground truth images, while the remaining rows display rendering results.

TABLE 11: The Number of available images Obtained by Different Methods.

Scene	COLMAP				Meshroom				AprilTag			
	Ball	HalfBall	Room	Array	Ball	HalfBall	Room	Array	Ball	HalfBall	Room	Array
Computer	2	2	2	100	3	37	26	99	110	100	88	100
Ficus	2	2	2	2	8	9	21	100	100	110	100	100
Gate	16	31	31	98	41	67	34	100	110	100	88	100
Lego	48	92	86	100	54	99	88	100	110	100	88	100
Materials	38	2	71	5	36	0	36	0	110	100	88	100
Snowtruck	33	96	28	100	63	97	84	100	110	100	88	100
Statue	2	20	31	100	14	56	65	100	110	100	88	100
Train	37	93	47	100	49	100	84	100	110	100	88	100
Total Number	110	100	88	100	110	100	88	100	110	100	88	100

TABLE 12: Comparison Results between Two SFM-based Composite Methods and MC-NeRF.

Scene	PSNR $\uparrow$				SSIM $\uparrow$				LPIPS $\downarrow$				
	Ball	HalfBall	Room	Array	Ball	HalfBall	Room	Array	Ball	HalfBall	Room	Array	
COLMAP+NeRF	Computer	-	-	-	18.5081	-	-	-	0.8906	-	-	-	0.1677
	Ficus	-	-	-	-	-	-	-	-	-	-	-	-
	Gate	-	25.3121	21.1899	23.0474	-	0.9099	0.8889	0.9137	-	0.1206	0.2163	0.1195
	Lego	20.8396	21.8068	22.2283	18.8225	0.9189	0.9074	0.8075	0.8749	0.1446	0.0494	0.1859	0.1936
	Materials	22.5298	-	23.0754	-	0.8982	-	0.9577	-	0.1143	-	0.0957	-
	Snowtruck	12.7945	26.4260	-	18.4196	0.7328	0.9155	-	0.8695	0.3671	0.0884	-	0.2072
	Statue	-	-	22.1310	18.6054	-	-	0.9243	0.8903	-	-	0.1265	0.1205
	Train	13.2663	27.0967	20.9158	18.4150	0.7214	0.9371	0.8816	0.8847	0.4036	0.0614	0.1205	0.1937
	Mean	18.7213	25.1604	21.7981	19.4620	0.8499	0.9175	0.8920	0.8866	0.2087	0.0799	0.1490	0.1871
Meshroom+NeRF	Computer	-	-	-	21.5518	-	-	-	0.9081	-	-	-	0.0978
	Ficus	-	-	-	20.0217	-	-	-	0.9494	-	-	-	0.0990
	Gate	17.8344	20.8989	22.219	21.3296	0.8807	0.8804	0.9110	0.9257	0.1852	0.2550	0.1642	0.2277
	Lego	15.4833	18.3328	13.4810	22.2046	0.7851	0.7856	0.7227	0.9110	0.3341	0.2550	0.4191	0.1117
	Materials	20.6267	-	-	-	0.9293	-	-	-	0.0998	-	-	-
	Snowtruck	13.2374	16.9954	10.1618	19.4415	0.8998	0.8189	0.6761	0.9166	0.1758	0.2526	0.5043	0.1138
	Statue	-	22.9819	14.1917	-	-	0.9684	0.8227	-	-	0.0547	0.2509	-
	Train	21.1296	17.8849	11.8588	21.8684	0.8911	0.7979	0.6913	0.9237	0.1323	0.2526	0.4561	0.0997
	Mean	16.7955	19.4188	14.3824	21.0696	0.8737	0.8502	0.7647	0.9224	0.1987	0.1920	0.3589	0.1249
MC-NeRF	Computer	24.2311	23.0962	23.6603	24.6946	0.9217	0.8876	0.9008	0.9395	0.0794	0.0933	0.1004	0.0444
	Ficus	24.9479	24.7662	26.5778	24.2929	0.9488	0.9070	0.9386	0.9504	0.0336	0.0519	0.0449	0.0387
	Gate	27.9102	26.0876	29.3081	26.7734	0.9333	0.9131	0.9250	0.9356	0.0519	0.0525	0.0602	0.0439
	Lego	24.1226	23.4818	23.3858	24.3502	0.9227	0.8682	0.8837	0.9629	0.0620	0.0901	0.0874	0.0343
	Materials	26.8742	26.6170	27.1323	25.0106	0.9484	0.9488	0.9529	0.9601	0.0321	0.0423	0.0294	0.0397
	Snowtruck	24.8742	24.0678	23.4415	23.3363	0.9211	0.8882	0.8937	0.9375	0.0433	0.0882	0.0874	0.0451
	Statue	28.6882	29.2767	28.7953	24.6619	0.9731	0.9670	0.9612	0.9651	0.0303	0.0301	0.0398	0.0281
	Train	23.3830	23.5271	22.2576	23.4073	0.9311	0.8773	0.8589	0.9395	0.0454	0.0991	0.0835	0.0507
	Mean	25.6289	25.1151	25.5698	24.5659	0.9375	0.9072	0.9144	0.9488	0.0473	0.0684	0.0666	0.0406



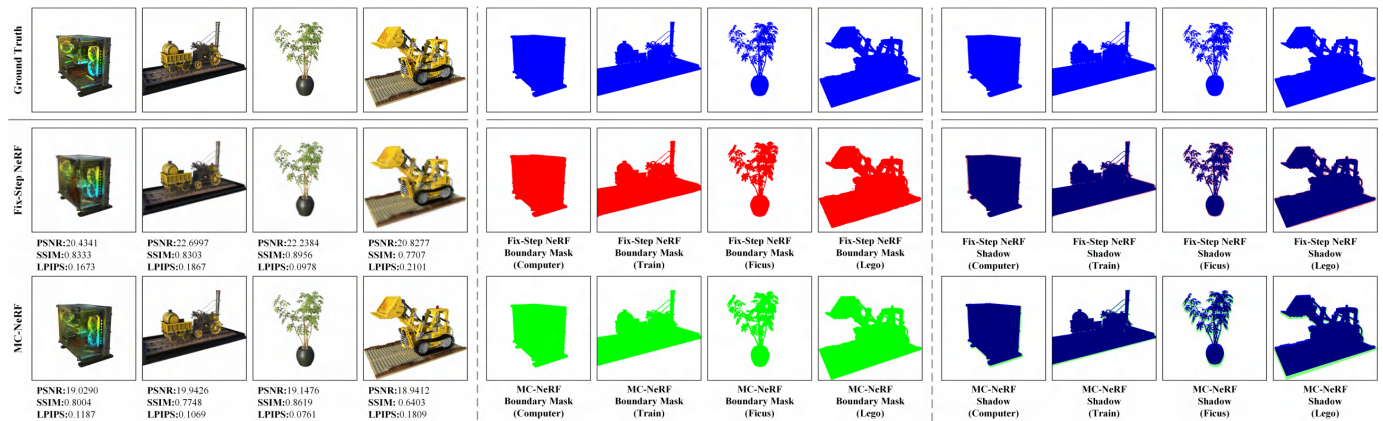


Fig. 17: Boundary alignment results for rendering objects. On the left, the rendering results and evaluation metrics for Fix-Step NeRF and MC-NeRF are displayed. In the middle section, the object boundary masks are presented. On the right, the comparison results between the object boundaries and the ground truth are shown. It can be observed that Fix-Step NeRF exhibits better object alignment performance compared to MC-NeRF. The more pixels contained within the mask, the more favorable it is for evaluation methods like PSNR, which involve pixel-to-pixel calculations.